



<https://technobius.kz/>

e-ISSN  
3007-0147

# Technobius Physics

*A peer-reviewed open-access journal*

*Technobius, LLP*

*Volume 2, No. 2, 2024*



# Technobius Physics

Volume 2, No. 2, 2024



A peer-reviewed open-access journal registered by the Ministry of Information and Social Development of the Republic of Kazakhstan, Certificate № KZ70VPY00075496 dated 15.08.2023




**ISSN (Online):** 3007-0147

**Thematic Directions:** General Physics, Condensed Matter Physics

**Publisher:** Technobius, LLP

**Address:** 2 Turkestan street, office 116, 010000, Astana, Republic of Kazakhstan

















## Editor-in-Chief:

   *Aida Nazarova*, PhD, Laboratory Assistant, Department of Physics, Nazarbayev University, Astana, Kazakhstan

## Technical Editor:

   *Saeed Nasiri*, Dr, Professor, Department of Physics, Nazarbayev University, Astana, Kazakhstan

## Editors:

-   *Sang Ma Lee*, Dr., Professor, Engineering Research Center for Net Shape and Die Manufacturing, Pusan National University, Busan, South Korea
-   *Suk Bong Kang*, Dr., Professor, Korea Institute of Materials Science, Changwon, South Korea
-   *Marshall Onellion*, Dr., Professor, Department of Physics, University of Wisconsin-Madison, Madison, United States
-    *Bill Wheatle*, Dr, Assistant Professor, McKetta Department of Chemical Engineering, The University of Texas at Austin, Austin, United States
-   *Hyun-ho Kim*, Dr, Assistant Professor, School of Mechanical Engineering, Pusan National University, Busan, South Korea
-   *Yong-phil Jeon*, Dr., Precision Manufacturing System Division, Pusan National University, Busan, South Korea
-    *Marius Schwarz*, Dr., Assistant Professor, Department of Civil Engineering, University North, Varaždin, Croatia

**Copyright:** © Technobius, LLP

**Contacts:** Website: <https://technobius.kz/>  
E-mail: [technobiusphysics@gmail.com](mailto:technobiusphysics@gmail.com)

**CONTENTS**

| <b>Title and Authors</b>  | <b>Category</b>                 | <b>No.</b> |
|---|---------------------------------|------------|
| Probing molecular architectures and interactions with scanning tunneling microscopy on graphite and arachidic acid functionalized surfaces<br><i>Medet Mustafin</i> | <i>Condensed Matter Physics</i> | 0010       |
| Optimizing ultrasound Doppler measurement precision: a comprehensive experimental approach<br><i>Alima Aidarbek</i>   | <i>General Physics</i>          | 0011       |
| Spectral characterization of elemental emissions, experimental insights and theoretical evaluation<br><i>Islam Amangeldinov, Dmitri Korovaev</i>                    | <i>General Physics</i>          | 0012       |
| Comprehensive analysis of solar cell behavior: effects of light intensity, temperature, and operational modes<br><i>Ersaiyn Bekbolsynov</i>                         | <i>General Physics</i>          | 0013       |
| Cooling and heating innovations: exploring the diverse applications of heat pumps<br><i>Karina Mussabekova, Aliya Nurbayeva</i>                                     | <i>General Physics</i>          | 0014       |



## Probing molecular architectures and interactions with scanning tunneling microscopy on graphite and arachidic acid functionalized surfaces

 Medet Mustafin\*

Department of Physics and Technology, Al-Farabi Kazakh National University, 71 Al-Farabi ave., Almaty, Kazakhstan

\*Correspondence: [medet.mustafin.01@mail.ru](mailto:medet.mustafin.01@mail.ru)

**Abstract.** This study investigates the application of scanning tunneling microscopy in exploring molecular structures and interfaces relevant to nanotechnology. Graphite was selected as a sample due to its ease of visualization of atomic arrangements and surface inertness. The surface of highly oriented pyrolytic graphite treated with arachidic acid ( $C_{20}H_{32}O_2$ ) was examined to gain insights into the behavior of organic molecules at liquid-solid interfaces. Through detailed observations, the study demonstrates the versatility of scanning tunneling microscopy in elucidating molecular architectures and interactions. The findings underscore the importance of scanning tunneling microscopy in advancing our understanding of molecular systems and driving progress in nanotechnology applications. This work highlights the pivotal role of scanning tunneling microscopy in unraveling the complexities of nanoscale phenomena and fostering future innovations in the field.

**Keywords:** scanning tunneling microscopy, graphite, molecular structures, liquid-solid interfaces, nanotechnology applications

### 1. Introduction

Solid surface atomic composition can be observed with a Scanning Tunneling Microscope (*STM*). These compositions affect the dynamics of the solid, which makes them significant in material physics [1-2]. Quantum tunneling is the foundation of *STM* operation. The quantum mechanical tunneling effect is the fundamental idea that drives *STM* [3-4]. The ability of particles to pass over potential barriers that are taller than their total energy is described by this phenomena. The properties of particle waves are intimately related to the tunneling effect. A model of the energy levels of free electrons in a metal can explain this phenomena [5-6]. The energy of electrons can be expressed by the formula:

$$E = \frac{p^2}{2m} \quad (1)$$

Where,  $p$  is the electron's momentum and  $m$  is its mass, because the electron gas inside the conductor is regarded as free in this model. The Fermi level is the greatest energy an electron can have in a metal at zero temperature [7]. Conduction electrons could potentially find a trench throughout the metal's entire volume. The electrons with the highest energy, or those around Fermi level, are the ones that primarily contribute to the tunnel current. Conduction electrons are located at the edge of the potential well, which acts as a potential barrier for them at the metal surface and the boundary between the metal and vacuum. The output work  $\phi$  determines the height of this potential barrier.

*STM* under ultrahigh vacuum conditions allows obtaining atomic images of the surface of metals and semiconductors, including silicon, by registering the tunneling current between the probe and the surface under study close to it. It is designed to study elementary structural processes on the surface of semiconductors and metals to create nanosystems and new materials with unique

properties. Not only may *STM* be used in ultra-high vacuum, but it can also be employed at temperatures ranging from almost 0 K to more than 1000 °C in air, water, and other liquids or gases with ambient temperatures [8].

Many of the present and future uses of nanotechnology, such as molecular light-harvesting and emitting devices, molecular electronics, biological identification, and molecular sensor technologies, are based on organic molecules [9]. Systems based on molecular thin films are emerging as a very promising path for the near future, whereas single-molecule electronics pose considerable obstacles for practical applications. One prominent technique for developing new molecular architectures is self-assembly, especially when it comes to the production of electrical and optoelectronic devices.

## 2. Methods

In this work, graphite was chosen as a sample for *STM* studies due to the ease of visualization of its atoms and the inertness of its surface. Since each crystallite in synthetic highly oriented pyrolytic graphite (*HOPG*) is perfectly aligned, it is utilized in place of natural graphite. The graphite topographic image presented in Figure 1 has a distinctive hexagonal pattern that is distinct from the honeycomb pattern [10]. This effect is caused by the electrical structure's quirks, which cause only every other atom to be mapped. Because the electron density is focused closer to the bulk, the carbon atoms on the surface, which are positioned above other atoms of the second carbon layer, are not visible [11].

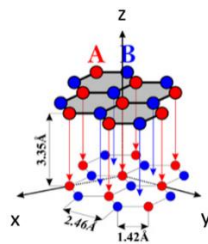


Figure 1 – Graphite's 3D atomic structure

When an electric field is applied to an extremely sharp metal tip in close proximity to an electrically conductive sample, a current flows between the tip and the sample without any physical contact. Using this so-called tunneling current, the electrical topography of the surface of freshly produced graphite is examined on the supplementary nanometer scale. Atoms and hexagonal structures are photographed by scanning the graphite surface line by line with the tip line. The main part of the equipment is scanning, based on a platform for vibration isolation and a protective magnetic cover for tip and sample inspection. Without the necessity for mechanical contact, a current can be produced between a sharp metal tip and an electrically conductive sample when an electric field is introduced. This phenomenon, called tunneling current, is utilized to examine the surface electron topography of freshly manufactured graphite at an additional nanoscale scale. Atoms and hexagonal structures are photographed through the application of a tip line over the graphite surface.

Figure 2 *a* presents a piezo-elements enable metal tip, which move across a sample's surface during *STM*.

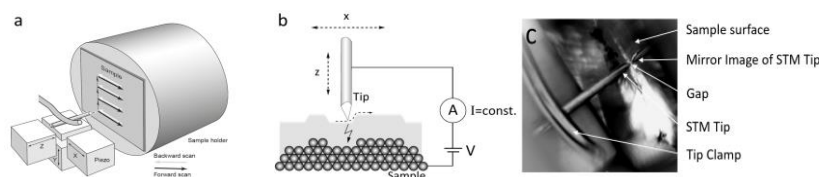


Figure 2 – *STM* sample mounted scheme

In Figure 2 *b* and *c* the tunneling current at which the tip is held is determined by the feedback loop *z*'s operational point. In essence, this establishes the separation between the tip and the model. The tip is nearer the sample surface the higher the set point. 5 nA is typically utilized for graphite atomic resolution.

By varying the voltage, these elements can precisely move the tip at a scale of picometers since they change length in reaction to applied voltage. A tunneling current is created across the tiny gap between the tip and the sample by an applied bias voltage. Constant-current or constant-height modes can be used for surface scanning. The tunneling current in the constant-height mode changes according to the tip's lateral position. The more widely used constant-current mode produces a profile of the sample's height based on the *z*-signal by using a feedback loop to maintain the tip height and keep the tunneling current constant. The tunneling current and distance have an exponential connection (a change of one Angström in distance results in a tenfold change in tunneling current) and the piezo-elements' exact movement allows for an extraordinary resolution, all the way down to the atomic level.

The *P*, *I* and *D* coefficients used in proportional-integral-differential (*PID*) controllers determine how the system reacts to deviations of the measured current from the set point. The number of values that are too low can cause the tip to be insufficiently sensitive to changes in height, while values that are too high can cause tip position fluctuations. Recommended parameter *D* can be set to zero. The values of parameters *P* and *I* was selected based on the current context and system response time. The default value of 1000 is a precise starting value.

The tip voltage indicates the offset applied to the tip. The lower the voltage, the closer the tip is to the surface. The optimum value of the bias voltage depends on the electronic structure of the sample, such as the density of states (*DOS*). For semiconductors, it is important to keep in mind that it is not recommended to place the bias voltage inside the band of forbidden energy states.

The *HOPG* surface was scanned at *STM* in air, which allowed imaging of different sizes, ranging from  $\sim 100$  nm, where step edges are visible, to as small as  $\sim 5$  nm with atomic resolution. The following characteristics of 5 nA, 0.6 nA, 1.3 V have been used for atomic resolution.

For more detailed analysis of a liquid-solid interface, we investigated the surface of *HOPG* treated with arachidic acid  $C_{20}H_{32}O_2$ .

### 3. Results and Discussion

Figure 3 presents the topography surface of the synthetic graphite scanned by *STM*. A scanning probe microscope provides an image of a surface magnified in all three dimensions: *x*, *y* and *z*, with maximum resolution in each axis. *x* –axis have been selected 1.2 nA,  $P_{gain}$  1200,  $I_{gain}$  1500., with the maximum resolution for each axis determined by various factors. The *z*-axis resolution is limited, first, by the sensitivity of the sensor and, second, by the amplitude of the probe vibrations relative to the sample surface. The design of the microscope must be able to reduce the amplitude of these vibrations to fractions of an angstrom.

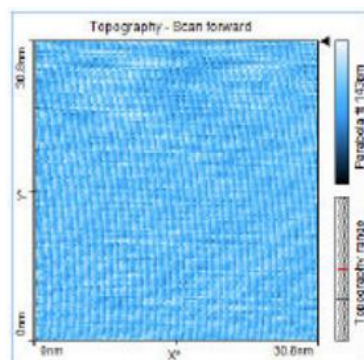


Figure 3 – Topography surface of 30 nm, scanned in 0.14 s, with 1.2 nA,  $P_{gain}$  1200,  $I_{gain}$  1500

Since thermal fluctuations have an impact on nanoscale measurements, we have selected a mode of 0.03 s at 128 "Points/Line" for atomic resolution in order to scan the sample as quickly as possible. Since that four to eight atoms have a diameter of one nanometer, much smaller picture sizes are required to reach atomic resolution. On Figure 4, atomic arrangements are often identifiable at image sizes of roughly 10–3 nm. Consequently: In the imaging panel, set the image size to 3 nm (Figure 5).

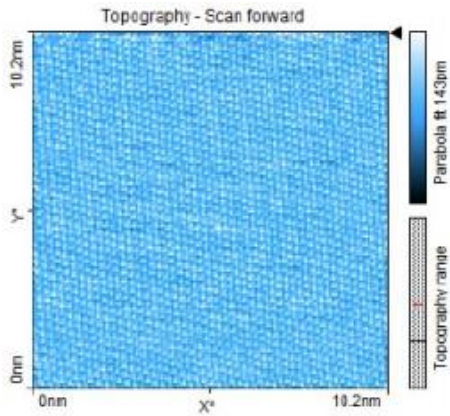


Figure 4 – Topography surface of 10 nm, scanned in 0.03 s, with 1.2 nA,  $P_{gain}$  1200,  $I_{gain}$  1500

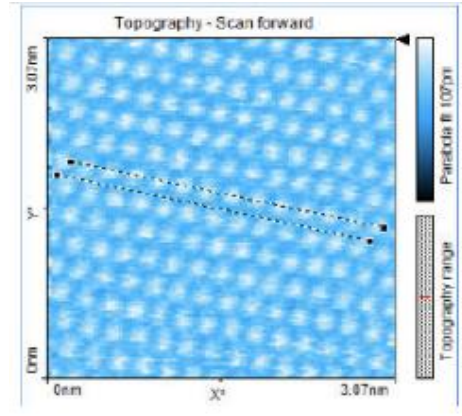


Figure 5 – Topography surface of 3 nm, scanned in 0.03 s, with 1.2 nA,  $P_{gain}$  1300,  $I_{gain}$  850. Line-to-line distance:  $d=138$  pm

To investigate the interface between the liquid-solid interface, we applied arachidic acid  $C_{20}H_{32}O_2$  to the *HOPG*. Figure 6a shows the condition of the test sample applied with arachidic acid. Parameters for scanning were as follows 0.6 nA, 1.3 V, image size  $15.8 \times 15.8 \text{ nm}^2$ . The scanned image on Figure 6b showed that at fine resolution, the obvious features of arachidic acid, which has an orange coloration, dominate. However, at the same parameters, it is almost impossible to distinguish individual carbon atoms.

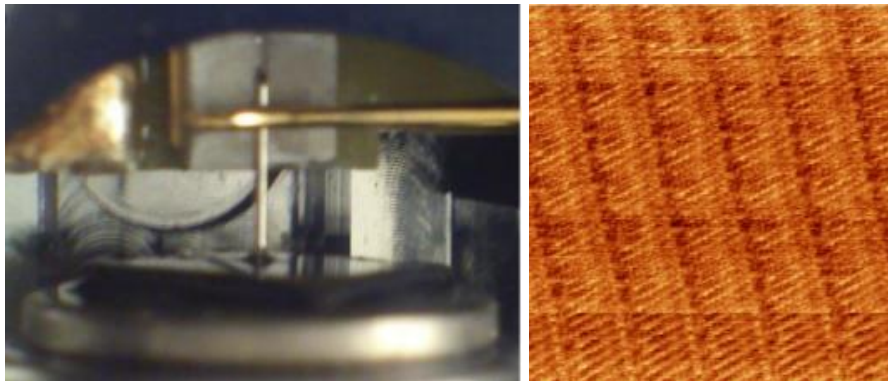


Figure 6 – Applying acid  $C_{20}H_{32}O_2$  on *HOPG* surface: a) test sample; b) scanned image

#### 4. Conclusions

In conclusion, this study demonstrates the versatility and potential of *STM* in investigating various interfaces and molecular structures. By utilizing graphite as a sample, the ease of visualizing atomic arrangements and the inert surface nature facilitated detailed observations. Furthermore, the exploration of the *HOPG* surface treated with arachidic acid provided insights into the behavior of organic molecules at liquid-solid interfaces. These findings underscore the significance of *STM* in advancing our understanding of molecular structures and their interactions, paving the way for further developments in nanotechnology applications, such as molecular electronics, optoelectronic devices,

and sensor technologies. Overall, this work highlights the crucial role of *STM* in unraveling the complexities of molecular systems and driving advancements in the field of nanoscience.

### References

1. Photoelectrochemical cells / M. Grätzel // Nature. — 2001. — Vol. 414, No. 6861. — P. 338–344. <https://doi.org/10.1038/35104607>
2. Surface Characterization of Materials at Ambient Conditions by Scanning Tunneling Microscopy (STM) and Atomic Force Microscopy (AFM) / S.N. Magonov // Applied Spectroscopy Reviews. — 1993. — Vol. 28, No. 1–2. — P. 1–121. <https://doi.org/10.1080/05704929308021499>
3. Scanning Microscopy for Nanotechnology: Techniques and Applications / W. Zhou, Z.L. Wang. — Berlin, Germany: Springer Science & Business Media, 2007. — 533 p.
4. Study of superconductors by electron tunneling / I. Giaever, K. Megerle // Physical Review. — 1961. — Vol. 122, No. 4. — P. 1101–1111. <https://doi.org/10.1103/PhysRev.122.1101>
5. Phonon induced tunneling of ions in solids / J.A. Sussmann // Physik der Kondensierten Materie. — 1964. — Vol. 2, No. 2. — P. 146–160. <https://doi.org/10.1007/BF02422872>
6. Energy distributions of field emitted electrons / R. Stratton // Physical Review. — 1964. — Vol. 135, No. 3A. — P. A794–A805. <https://doi.org/10.1103/PhysRev.135.A794>
7. Effects of disorder and temperature on Fermi-energy of one-dimensional disordered systems / Sh. Shang Ma, X. Liu, H. Xu, Y.-F. Li // Journal of Central South University. — 2007. — Vol. 38, No. 2. — P. 281–284 .
8. A low temperature, ultrahigh vacuum, microwave-frequency-compatible scanning tunneling microscope / S.J. Stranick, M.M. Kamna, P.S. Weiss // Review of Scientific Instruments. — 1994. — Vol. 65, No. 10. — P. 3211–3215. <https://doi.org/10.1063/1.1144551>
9. Microtechnology, nanotechnology, and the scanning-probe microscope: an innovative course / J.D. Adams, B.S. Rogers, L.J. Leifer // IEEE Transactions on Education. — 2004. — Vol. 47, No. 1. — C. 51–56. <https://doi.org/10.1109/TE.2003.817623>
10. Topographic modifications on the graphite surface induced by high energy single-ion impact / C.H. de Villeneuve, M. Phaner, L. Porte, N. Monocoffre, P. Pertosa, J. Tousset // Vacuum. — 1990. — Vol. 41, No. 7–9. — P. 1686–1689. [https://doi.org/10.1016/0042-207X\(90\)94055-U](https://doi.org/10.1016/0042-207X(90)94055-U)
11. X-ray topographic determination of the granular structure in a graphite mosaic crystal: A three-dimensional reconstruction / M. Ohler, M. Sanchez Del Rio, A. Tuffanelli, M. Gambaccini, A. Taibi, A. Fantini, G. Pareschi // Journal of Applied Crystallography. — 2000. — Vol. 33, No. 4. — P. 1023–1030. <https://doi.org/10.1107/S0021889800005975>

### Information about author:

*Medet Mustafin* – Master Student, Department of Physics and Technology, Al-Farabi Kazakh National University, 71 Al-Farabi ave., Almaty, Kazakhstan, [medet.mustafin.01@mail.ru](mailto:medet.mustafin.01@mail.ru)

### Author Contribution:

*Medet Mustafin* – concept, methodology, resources, data collection, testing, modeling, analysis, visualization, interpretation, drafting, editing, funding acquisition.

**Conflict of Interest:** The authors declare no conflict of interest.

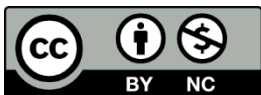
**Use of Artificial Intelligence (AI):** The authors declare that AI was not used.

*Received:* 20.11.2023

*Revised:* 02.03.2024

*Accepted:* 11.03.2024

*Published:* 17.04.2024



**Copyright:** © 2024 by the authors. Licensee Technobius, LLP, Astana, Republic of Kazakhstan. This article is an open access article distributed under the terms and conditions of the Creative Commons Attribution (CC BY-NC 4.0) license (<https://creativecommons.org/licenses/by-nc/4.0/>).





## Optimizing ultrasound Doppler measurement precision: a comprehensive experimental approach

 Alima Aidarbek\*

School of Natural Sciences, Astana International University, 8 Kabanbay ave., Astana, Kazakhstan

\*Correspondence: [alima.aidarbek@mail.ru](mailto:alima.aidarbek@mail.ru)

**Abstract.** Experimental studies were conducted utilizing advanced equipment comprising a generator, tubing system, pump module, sonographer, and PC. The generator serves as the central component connected by tubes to the pump, forming a closed circuit. A tee in the tubing set prevents Doppler fluid leakage, with the fluid poured through a special funnel into the circuit post-connection. The Doppler fluid is evenly mixed by shaking its bottle to enhance signal strength. The entire system is sealed. The centrifugal pump generates continuous flows; different power modes were tested for 30 minutes each, with frequency shifts measured at angles  $\alpha=15^\circ$ ,  $30^\circ$ , and  $60^\circ$ . Pump disconnection from the power supply prevents liquid entry during tubing connection. The pump module housing includes ventilation holes. A 3 by 8 cm Doppler prism, treated with ultrasonic gel, was connected to the tubing to capture data. A sonographer emitting signals at 2 MHz, with a gain range of 10 to 40 dB, was utilized for sound spectra analysis. High-mode operation, 4 microseconds pulse duration, and a 32 microseconds receiver gate were set. The ultrasound apparatus dimensions were 230 x 236 x 168 mm, with a power consumption of 27 VA. Data visualization was facilitated by an LED panel, with adjustable acoustic signal volume. A USB interface enabled connection to a PC for ease of use and data analysis. Special software facilitated graph generation depicting frequency vs. time dependence measurements. Frequency analysis yielded average (f-mean) and maximum (f-max) frequency values, with f-mean utilized to measure Doppler effect frequency shift. The presented data showcases various pump speeds and incidence angles, each yielding distinctive frequency characteristics.

**Keywords:** ultrasonic, Doppler Effect, frequency shift, incidence angles, pump speed.

### 1. Introduction

In classical hydromechanics it is common to consider a fluid as a homogeneous medium. However, real environments surrounding us are most often heterogeneous, consisting of different components - liquid, solid and gaseous [1]. Examples of multiphase media are gas suspensions, aerosols, suspensions, emulsions, liquids with gas bubbles, composite materials, liquid-saturated soils, nanofluids and others. Interactions between phases can have a significant effect on flow dynamics, drag, and heat transfer [2]. For example, when flying at supersonic speeds in a dusty atmosphere, it is necessary to consider the effect of dust particles on the surface of the aircraft. When transporting hydrocarbons through pipelines, the presence of the gas phase can lead to the formation of plugs [3]. When it comes to the movement of blood through vessels, it is important to remember that blood is a multiphase medium in which plasma is the liquid phase and leukocytes, platelets, and red blood cells are suspended solids.

The description of motion in inhomogeneous media is a complex problem. To build a mathematical model, it is necessary to develop a technique for averaging flow parameters in such a way as to take into account several characteristic scales: molecular, macroscopic, and the scale corresponding to the size of inclusions [4]. Closure of the system of equations requires the development of models describing friction phenomena, energy transfer in different phases, and interphase interaction [5]. One of the most successful methods of analyzing the motion of moving

structures is the ultrasound Doppler Effect, which is widely used in medicine. There are two main approaches to its application: the continuous wave method and the pulsed-wave method [6]. While conventional Doppler detectors can only detect the presence of motion, directional or pulsed-wave Doppler systems provide results with a higher level of detail.

The application of ultrasound of all things has aroused some interest. For example, a group of scientists [7-9] used a method to determine the refractive index of isolated solids by immersing them in liquids with a predetermined refractive index. However, such an effective method is not always practical. Other scientists [10] have examined the relationship between acoustic attenuation and the reflection coefficient of longitudinal ultrasonic waves, where the main idea was to determine surface parameters using either of the ultrasonic or reflection coefficients with negligible error.

Recently, research has been actively conducted to improve the accuracy of distance and velocity measurements using Doppler ultrasound by improving data processing techniques. Of particular interest is the high-precision velocity and distance measurement technique, which includes a special signal processing algorithm that uses oversampling using two modulated waves [11].

Therefore, This study investigates strategies to improve the accuracy of distance measurement with an ultrasonic transducer using improved Doppler technology.

## 2. Methods

Experimental studies were carried out with advanced equipment consisting of several parts: generator, tubing system, pump module, sonographer and PC. The central part is the generator connected by tubes to the pump, which form a complete circuit. The tee of the tubing set was installed at the pump inlet point to prevent Doppler fluid from leaking out of the tee. Using a special funnel on the tee, the Doppler fluid is poured into the circuit once it is fully connected. The bottle of Doppler fluid is shaken to evenly mix the scattering particles. This procedure is necessary to obtain a stronger resultant signal during measurements. The entire system is completely sealed.

The centrifugal pump is capable of generating both continuous and pulsating flows. However, only continuous flows were used in this study. To generate continuous flows, the pump was operated in several modes for 30 minutes, depending on the % power fixed, which corresponds to the pump speed. For each speed, the frequency shift was measured at three different incidence angles ( $\alpha=15^\circ$ ,  $30^\circ$  and  $60^\circ$ ). When the tubing is connected, the pump is disconnected from the power supply to prevent liquid from entering the pump housing, which is especially important when filling the tubing system with liquid. The pump module housing is equipped with ventilation holes on the rear and bottom surfaces.

For this purpose, the sensor was connected to the corresponding prism surface. The 3 by 8 cm Doppler prism was mounted to the tubing using plates just behind one of its connectors, as these locations often experience vortices and flow turbulence. The transducer surfaces as well as the curved inner surface of the prism were treated with a special ultrasonic gel before installation to ensure good acoustic coupling and sufficient signal intensity between the prism and the tube.

A sonographer with a frequency range of 2 MHz emitted signals; a gain range varying from 10 to 40 dB was used to analyze the sound spectra. The power was determined by high mode of operation, with a pulse duration of 4 microseconds. The signal sampling volume was set to a high mode sampling volume with a full receiver gate of about 32 microseconds. The overall dimensions of the ultrasound apparatus were 230 x 236 x 168 mm, making it compact and mobile in use. The basic supply voltage of the device was standard 220 volts at a frequency of 50/60 Hz, and its power consumption is 27 volt-amperes (VA). To visualize the obtained data, the apparatus is equipped with an LED panel and also provides the possibility of adjusting the volume of the acoustic signal. To ensure ease of use and data analysis, the ultrasound pulsed Doppler device is equipped with an interface for connection to a personal computer via USB.

With the help of special software designed for visualization of data from the sonographer, graphs of frequency vs. time dependence measurement were obtained.

### 3. Results and Discussion

It is known that for sound waves, the observed frequency varies depending on whether the sound source is moving toward a resting observer or the observer is approaching a resting source. Figure 1 shows the current scattering intensity obtained from the sonographer. For deeper analysis of the received data it is necessary to perform decomposition of the signal into spectra (Figure 2). Based on the spectral analysis, two frequency characteristics are determined - the average value  $f$ -mean and the maximum value  $f$ -max. These values are determined and displayed. In the context of a Doppler experiment, the average frequency value ( $f$ -mean) is used as a measure of the frequency shift due to the Doppler Effect.

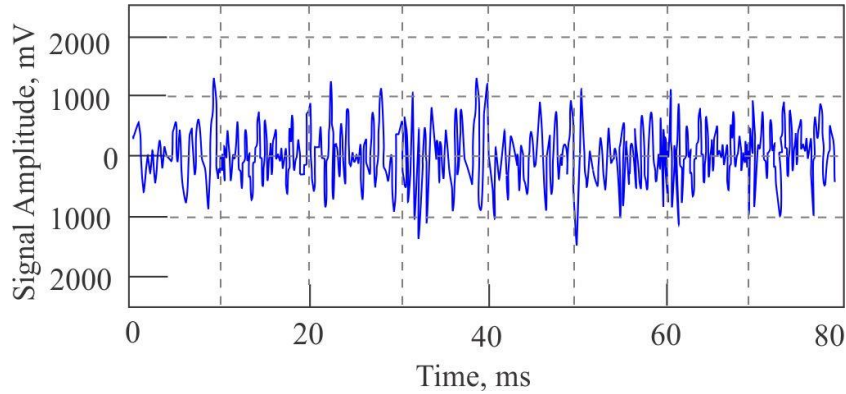


Figure 1 – Current scattering intensity of flow

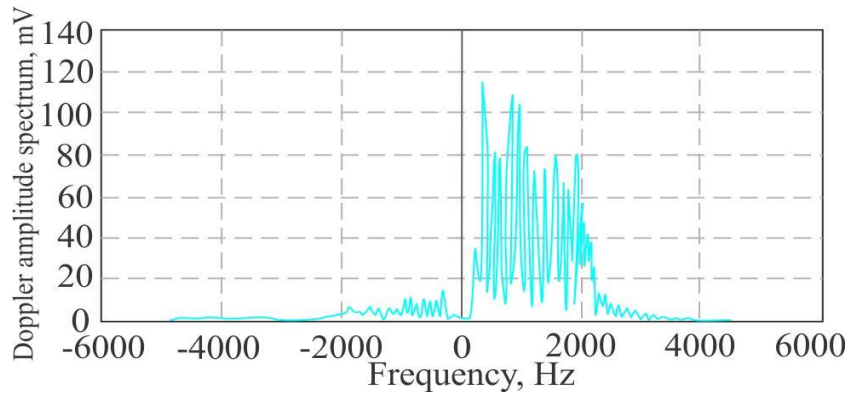


Figure 2 – Decomposition of the signal into spectra

Let us consider the process of the Doppler Effect in our pipe system, which is schematically represented in Figure 3. First of all, a pulse is generated along the fluid flow for a certain time  $T_1$  of its flow. At the same time, the second impulse is transmitted against the flow for the time fixed as  $T_2$ .

Using the resulting difference in pulse transit time  $\Delta t$ , the flow velocity  $v$  was calculated. As a result of the calculation, the volumetric flow rate was calculated based on the flow velocity and the cross section of the tube. Thus, using that  $c$  is the speed of sound in the medium, the following can be done:

$$c_1 = c + \vec{v} \cos \alpha \tag{1}$$

$$c_2 = c - \vec{v} \cos \alpha \tag{2}$$

$$\Delta t = T_2 - T_1 = \frac{L \vec{v} \cos \alpha}{c^2 - v^2 \cos^2 \alpha} \approx \frac{L \vec{v} \cos \alpha}{c^2} \tag{3}$$

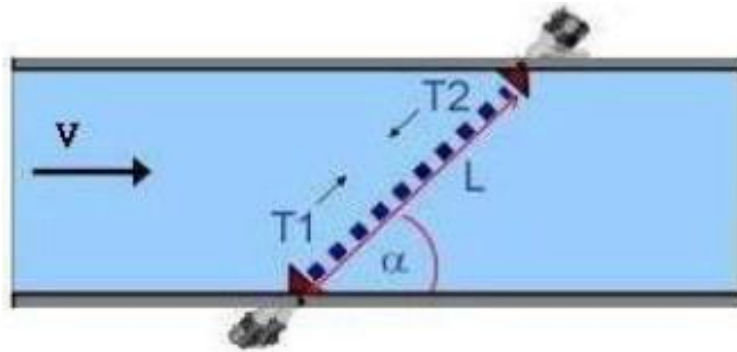


Figure 3 – The process of the Doppler effect in pipe system

In this case, it is important to take into account that the parameters of signal intensity  $I$ ,  $c$  и  $\cos\alpha$  must be known, and that the sound speed  $c$  is a function of the temperature of the medium, and this dependence must be taken into account in calculations or measurements.

This method has several advantages. Firstly, it allows measurements even with large cross-sections. Secondly, it does not require the construction of a special cross section. In addition, it allows measurements in non-conductive and contaminated liquids, which further extends the scope of its application and provides ease of use. However, it should be considered that the use of clamp-on sensors allows measurements to be made in reflection mode Figure 4. That is, the Doppler method measures the frequency shift that occurs when a sound wave scatters on small particles or impurities. Thus, the incident ultrasonic wave with a certain frequency on a moving object leads to a frequency shift  $f_0$ .

When the velocity of an object  $v$  is negligible compared to the speed of sound  $c$  in the medium, the following occurs:

$$\Delta f = f_0 \frac{v}{c} (\cos\alpha - \cos\beta) \tag{4}$$

Where:  $\alpha$  and  $\beta$  are angles between  $v$  and the wave normal. For a pulsed echo system with an ultrasonic transmitter, where the transmission and reflection coefficients are equal  $\alpha = \beta$ , hence:

$$\Delta f = 2 f_0 \frac{v}{c} \cos\alpha \tag{5}$$

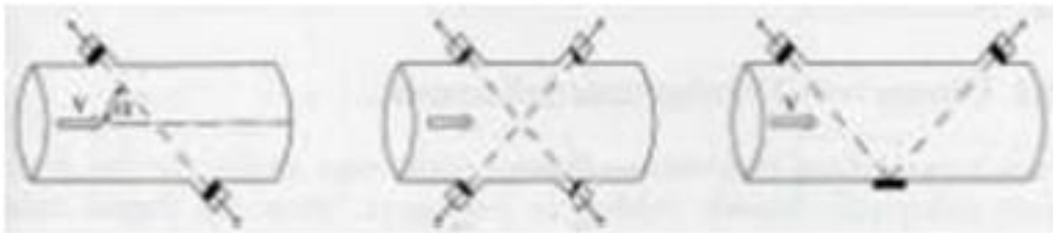


Figure 4 – Scheme of flow in the pipe cross-section

When calculating by formula (2), it is necessary first of all to determine the Doppler angle  $\alpha$ , which is determined by the angle of incidence  $\alpha_p$  on the prism.

When sound propagates from the prism into the liquid, the angle changes according to the law of refraction and depends on different sound velocities. The tube wall is assumed to be a plane-parallel layer, which allows it to be omitted in the calculations. According to the law of refraction, the Doppler angle can be calculated as follows:

$$\alpha = 90^\circ - \arcsin\left(\sin\alpha_p \frac{c_L}{c_P}\right) \tag{3}$$

Where:  $\alpha_p$  – denotes the angle of incidence,  $C_p$  – denotes the speed of sound in the prism, and  $C_L$  – denotes the speed of sound in the fluid. Using formulas 2 and 3, the flow characteristics presented in Table 1 were calculated.

Table 1 – Calculated flow characteristics

| Pump, % | Angle, ° | F – mean, Hz | Doppler angle $\alpha$ , | $\cos \alpha$ , ° | $v, \frac{sm}{s}$ |
|---------|----------|--------------|--------------------------|-------------------|-------------------|
| 30      | 15       | 185          | 80.0                     | 0.17              | 47.71             |
| 50      | 15       | 285          | 80.0                     | 0.17              | 73.50             |
| 70      | 15       | 405          | 80.0                     | 0.17              | 104.45            |
| 30      | 30       | 342          | 70.3                     | 0.34              | 45.66             |
| 50      | 30       | 515          | 70.3                     | 0.34              | 68.75             |
| 70      | 30       | 700          | 70.3                     | 0.34              | 93.45             |
| 30      | 60       | 570          | 54.3                     | 0.58              | 43.93             |
| 50      | 60       | 920          | 54.3                     | 0.58              | 70.91             |
| 70      | 60       | 1320         | 54.3                     | 0.58              | 101.74            |

Figures 5 and 6 show the dependence of Doppler shift on frequency and velocity, respectively, for set angles of 15 30 and 60 degrees.

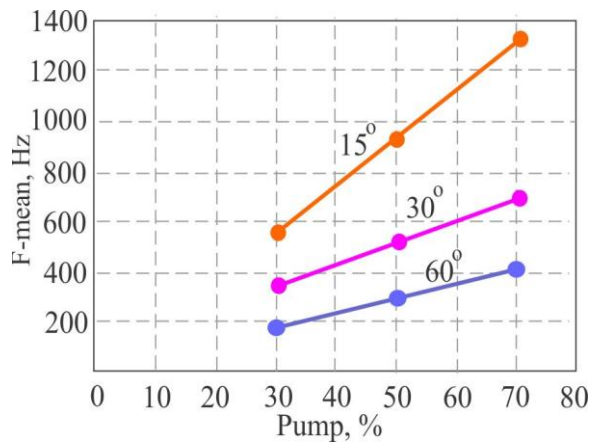


Figure 5 – Dependence of Doppler shift on frequency

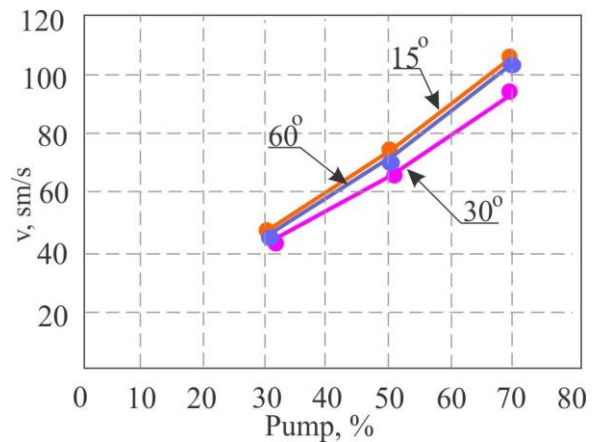


Figure 6 – Dependence of Doppler shift on velocity

Figure 3 demonstrates that the Doppler frequency shift increases with increasing pump speed as well as decreasing Doppler angle. A similar increase in shift is observed for all angle values between 15 and 60 degrees. Figure 4 shows the calculated velocity, which demonstrates that for any given velocity, the coefficient  $\Delta f/\cos(\alpha)$  remains nearly constant, indicating that there is no measurement error as a function of angle.

#### 4. Conclusions

In conclusion, the experimental investigation conducted with advanced equipment, including a generator, tubing system, pump module, sonographer, and PC, and provided valuable insights into the Doppler Effect phenomenon. The meticulous design and operation of the experimental setup ensured accurate measurements and robust data acquisition. Through careful control of pump speed and Doppler angles, the study systematically explored the relationship between Doppler frequency shift and varying experimental parameters. The results revealed significant trends, including an increase in the Doppler frequency shift with higher pump speeds and decreasing Doppler angles 15°, 30°, 60°. Furthermore, the analysis demonstrated the consistency of the coefficient  $\Delta f/\cos(\alpha)$  across different velocities, indicating the absence of measurement errors as a function of angle. Overall, these findings contribute to a deeper understanding of the Doppler Effect and its implications in fluid dynamics research and medical diagnostics. The comprehensive methodology and rigorous data analysis underscore the reliability and significance of the experimental findings presented in this study.

## References

1. Ultrasonic Doppler Technique for Application to Multiphase Flows: A Review / Ch. Tan, Yu. Murai, W. Liu, Y. Tasaka, F. Dong, Y. Takeda // International Journal of Multiphase Flow. — 2021. — V. 144. — P. 103811. <https://doi.org/10.1016/j.ijmultiphaseflow.2021.103811>
2. Non-invasive classification of gas–liquid two-phase horizontal flow regimes using an ultrasonic Doppler sensor and a neural network / B.M. Abbagoni, H. Yeung // Measurement Science and Technology. — 2016. — Vol. 27, No. 8. — P. 4002. <https://doi.org/10.1088/0957-0233/27/8/084002>
3. Estimation of volume fractions and flow regime identification in multiphase flow based on gamma measurements and multivariate calibration / B.K. Arvoh, R. Hoffmann, M. Halstensen // Flow Measurement and Instrumentation. — 2012. — Vol. 23, No. 1. — P. 56–65. <https://doi.org/10.1016/j.flowmeasinst.2011.11.002>
4. Doppler effect-based fiber-optic sensor and its application in ultrasonic detection / F. Li, M. Hideaki, K. Kazuro, Sh. Takehiro // Optical Fiber Technology. — 2009. — Vol. 15, No. 3. — P. 296–303. <https://doi.org/10.1016/j.yofte.2009.01.003>
5. The Effect of Amplitude Modulation on the Axial Resolution of Doppler-Based Ultrasonic Topography Measurement / J.R. Gatabi, S. Das, F. Forouzbakhsh // IEEE Transactions on Instrumentation and Measurement. — 2016. — Vol. 65, No. 12. — P. 2780–2786. <https://doi.org/10.1109/TIM.2016.2600999>
6. Effect of frequency analysis algorithms on velocity data using ultrasonic doppler method / R. Sakagami, H. Murakawa, S. Katsumi, T. Nobuyuki // ASME-JSME-KSME 2011 Joint Fluids Engineering Conference, AJK 2011. — 2011. — Vol. 1, No. PARTS A, B, C, D. — P. 2773–2780. <https://doi.org/10.1115/AJK2011-11021>
7. Ultrasonic measurements of surface roughness / G.V. Blessing, J.A. Slotwinski, D.G. Eitzen, H.M. Ryan // Applied Optics. — 1993. — Vol. 32, No. 19. — P. 3433–3437. <https://doi.org/10.1364/AO.32.003433>
8. Surface roughness evaluation via ultrasonic scanning // S.J. Oh, Y.C. Shin, E.S. Furgason // IEEE Trans Ultrason Ferroelectr Freq Control. — 1994. — Vol. 41, No. 6. — P. 863–871. <https://doi.org/10.1109/58.330267>
9. Ultrasonic evaluation of geometrical and surface parameters of rough defects in solids / M.D. Billy, F. Cohen-Ténoudji, G. Quentin, K. Lewis, L. Adler // Journal of Nondestructive Evaluation. — 1980. — Vol. 1, No. 4. — P. 249–261. <https://doi.org/10.1007/BF00571806>
10. Ultrasonic evaluation of surface roughness using normal incidence pulse echo technique / A.M. Addelhay, I.M.I. Mubark // e-Journal of Nondestructive Testing. — 2004. — Vol. 9, No. 4. — P. 3.
11. Ultrasonic distance and velocity measurement using a pair of LPM signals for cross-correlation method: Improvement of Doppler-shift compensation and examination of Doppler velocity estimation / S. Hirata, M.K. Kurosawa // Ultrasonics. — 2012. — Vol. 52, No. 7. — P. 873–879. <https://doi.org/10.1016/j.ultras.2012.02.007>

### Information about author:

*Alima Aidarbek* – Master Student, School of Natural Science, Astana International University, 8 Kabanbay ave., Astana, Kazakhstan, [alima.aidarbek@mail.ru](mailto:alima.aidarbek@mail.ru)

### Author Contribution:

*Alima Aidarbek* – concept, methodology, resources, data collection, testing, modeling, analysis, visualization, interpretation, drafting, editing, funding acquisition.

**Conflict of Interest:** The authors declare no conflict of interest.

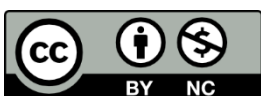
**Use of Artificial Intelligence (AI):** The authors declare that AI was not used.

*Received:* 13.02.2024

*Revised:* 15.04.2024

*Accepted:* 20.04.2024



*Published:* 22.04.2024



**Copyright:** © 2024 by the authors. Licensee Technobius, LLP, Astana, Republic of Kazakhstan. This article is an open access article distributed under the terms and conditions of the Creative Commons Attribution (CC BY-NC 4.0) license (<https://creativecommons.org/licenses/by-nc/4.0/>).



## Spectral characterization of elemental emissions, experimental insights and theoretical evaluation

 Islam Amangeldinov<sup>1,\*</sup>,  Dmitri Korovaev<sup>2</sup>

<sup>1</sup>Faculty of Engineering and Information Technology, Almaty Technological University, 100 Tole bi st., Almaty, Kazakhstan

<sup>2</sup>Institute of Physics, Technical University of Berlin, 17 Straße des, Berlin, Germany

\*Correspondence: [amangeldinovi@list.ru](mailto:amangeldinovi@list.ru)

**Abstract.** This experimental study delves into the spectral analysis of five discrete spectral lamps, namely helium, sodium, mercury, cadmium and zinc, utilizing a suite of scientific instrumentation including an optical spectrometer with converging lenses and a diffraction grating. The primary objective is to determine the wavelengths corresponding to visible spectral lines emitted by these lamps. Calibration of the spectrometer with the helium lamp facilitated the derivation of the diffraction grating constant. Subsequent measurements of diffraction angles allowed for the computation of experimental wavelengths, which were then compared with theoretical values. Analysis revealed slight discrepancies between experimental and theoretical values, likely attributed to systematic errors such as extraneous light sources and parallax errors in angle measurements. Furthermore, examination of spectral line splitting demonstrated the removal of degeneracy within specified energy levels, resulting in the observation of distinct spectral components. Overall, this study underscores the significance of meticulous experimental techniques in the elucidation of fundamental physical phenomena and highlights the interplay between theory and observation in spectral analysis.

**Keywords:** spectral analysis, spectral lamps, optical spectrometer, diffraction grating, wavelength determination.

### 1. Introduction

The study of hyperfine splitting in the spectra of ions, atoms, and molecules is a very urgent task both due to advances in the methods of modern spectroscopy and due to the development of theoretical methods of calculation.

The theoretical prediction of the hyperfine splitting constants and their comparison with measurement results is used to assess the level of accuracy of the calculation of the electronic wave function of the system under consideration. Precision calculations of the electronic structure are important for many tasks, ranging from the development of atomic clocks to the search for "new physics", such as the detection of the electron's electric dipole moment [1]. However, the study of superfine splitting is of independent interest also from the point of view of studying the structure of the nucleus. The point is that the effect of the finite size of the nucleus makes a significant contribution to the hyperfine splitting constant. The accounting of the charge part of this correction is not very difficult, since it depends mainly on the known charge radius of the nucleus. But the problem of accounting for the magnetic part of the correction is much more complicated and much more interesting [2-3].

In case of its successful solution, one can improve the agreement between the theoretical and experimental hyperfine splitting constants and draw conclusions about the differences in the distribution of the magnetization of isotope nuclei [4]. In addition, it is possible to determine the magnetic moments of short-lived nuclei. In contrast to stable nuclei, where it is possible to perform a nuclear magnetic resonance experiment, it is difficult to apply this experimental method for short-

lived nuclei. However, by combining the experimental constants of superfine splitting and the results of Bohr-Weisskopf effect calculations, it is possible to determine the desired magnetic moment [5–7].

In [8] and [9], an approach and programs were developed that allow one to calculate the Bohr-Weisskopf effect for neutral atoms both in the model of the nucleus with a uniform distribution of magnetization over its volume and in the Woods-Saxon model with the spin-orbit interaction taken into account while taking into account the effects of electron correlation. It should be noted that while the first model is widely used in atomic calculations, the second model was previously used only for multicharged ions, and for heavy neutral atoms it was applied for the first time. One of the difficulties encountered in the calculations was to take into account the effects of electron correlation. It turned out that for one of the electronic states of the thallium atom the value calculated at the Dirac-Hartree-Fock level differs from the experimental one by a factor of 5 [10]. Therefore, to achieve a good result, it is required to take into account the effects of electron correlation at a very high level, in the framework of the coupled cluster method with the inclusion of cluster amplitudes up to fourfold. One of the important results obtained in the course of this work was the refinement of the magnetic moments of a number of metastable thallium isotopes. The developed approach can also be generalized to the case of molecules, which is already becoming relevant.

## 2. Methods

In the conducted experimental investigation, a comprehensive array of scientific instrumentation was employed to determine the wavelengths corresponding to visible spectral lines originating from the elemental constituents contained within a series of 5 discrete spectral lamps. The instrumental setup encompassed an optical spectrometer featuring converging lenses, a diffraction grating, and a selection of spectral lamps comprising helium (He), sodium (Na), mercury (Hg), cadmium (Cd), and zinc (Zn). Additional equipment included a power supply and a lamp holder affixed to a tripod base.



Figure 1 – The instrumental setup of optical spectrometer

Prior to commencing the experimental procedure, the spectrometer underwent calibration utilizing the helium spectral lamp. The spectral emissions from the He lamp were captured, while concurrently determining the diffraction grating parameters. To facilitate this, the lamp was positioned within the lamp holder and allowed to stabilize for a duration of 5 minutes to attain optimal operational conditions. Subsequently, alterations to the diffraction angle facilitated the observation of light exhibiting diverse chromatic manifestations, with corresponding angular values documented



accordingly. A calibration curve, depicting the sinusoidal function of the angle against the wavelength of light, was then generated, facilitating the derivation of the diffraction grating constant.

In the ensuing phase of the experiment, the observable spectral lines emitted by sodium were measured. This involved the meticulous determination of the wavelengths characterizing the spectral lines of sodium, predicated upon the calculation of the corresponding angular values for each spectral line, utilizing the diffraction constant ascertained in the preceding calibration segment. The sodium spectral lamp was positioned within the lamp holder and situated before the spectrometer. Rotation of the telescopic apparatus enabled the sequential observation of diverse spectral hues, with angular rotations duly recorded. This protocol was iteratively applied to spectral lamps containing mercury, cadmium, and zinc, facilitating a comparative analysis of the obtained results vis-à-vis their theoretical counterparts.

### 3. Results and Discussion

In this paper we focused on observing and measuring the spectral lines emitted by different spectral lamps and determining the diffraction grating constant and the corresponding wavelengths corresponding to the brightest spectral lines. A helium lamp was taken for initial calibration and the values are shown in Table 1.

Table 1 – The spectral composition of helium (He)

| Color         | Literature wavelength, nm | Angle, degree | Angle error, minutes |
|---------------|---------------------------|---------------|----------------------|
| red           | 667.8                     | 23.72         | ±0.5                 |
| yellow        | 587.6                     | 20.77         | ±0.5                 |
| green         | 501.6                     | 17.67         | ±0.5                 |
| greenish blue | 492.2                     | 17.27         | ±0.5                 |
| bluish green  | 471.3                     | 16.57         | ±0.5                 |
| blue          | 447.1                     | 15.70         | ±0.5                 |

When an atom is placed in a magnetic field, its total energy is the sum of two parts: the internal energy of the atom and the energy of its interaction with the external magnetic field. The interaction energy is determined by the induction of the magnetic field and the magnetic moments (of both orbital and spin origin) of the electrons of the atom (we do not consider here the influence of the much smaller magnetic moment of the nucleus).

We investigated different spectral lamps and the data are shown in Table 2,3,4 and 5.

Table 2 – Determined visible spectral lines with corresponding angles from the sodium lamp (Na)

| Color         | $\lambda$ , nm | $\Delta\lambda$ , nm | Angle, degree | Angle error, min. |
|---------------|----------------|----------------------|---------------|-------------------|
| red           | 621.648        | 2.180                | 21.91         | ±0.5              |
| yellow        | 595.470        | 2.089                | 20.93         | ±0.5              |
| bluish green  | 571.856        | 2.006                | 20.07         | ±0.5              |
| greenish blue | 518.717        | 1.821                | 18.13         | ±0.5              |
| blue          | 502.564        | 1.765                | 17.55         | ±0.5              |
| purple        | 471.035        | 1.655                | 16.42         | ±0.5              |

Table 3 – Determined visible spectral lines with corresponding angles from the mercury lamp (Hg)

| Color        | $\lambda$ , nm | $\Delta\lambda$ , nm | Angle, degree | Angle error, min. |
|--------------|----------------|----------------------|---------------|-------------------|
| red          | 667.8          | 2.204                | 22.15         | ±0.5              |
| yellow       | 587.6          | 2.052                | 20.55         | ±0.5              |
| yellow       | 501.6          | 2.045                | 20.47         | ±0.5              |
| green        | 492.2          | 1.944                | 19.42         | ±0.5              |
| blue – green | 471.3          | 1.764                | 17.53         | ±0.5              |
| blue – green | 447.1          | 1.747                | 17.37         | ±0.5              |
| blue         | 432.5          | 1.557                | 15.40         | ±0.5              |
| violet       | 428.3          | 1.446                | 14.27         | ±0.5              |

Table 4 – Determined visible spectral lines with corresponding angles from the cadmium lamp (Cd)

| Color  | $\lambda$ , nm | $\Delta\lambda$ , nm | Angle, degree | Angle error,min. |
|--------|----------------|----------------------|---------------|------------------|
| red    | 667.8          | 2.277                | 22.93         | $\pm 0.5$        |
| red    | 587.6          | 2.233                | 22.47         | $\pm 0.5$        |
| green  | 501.6          | 1.833                | 18.25         | $\pm 0.5$        |
| green  | 492.2          | 1.805                | 17.97         | $\pm 0.5$        |
| blue   | 471.3          | 1.699                | 16.87         | $\pm 0.5$        |
| blue   | 447.1          | 1.668                | 16.55         | $\pm 0.5$        |
| violet | 432.5          | 1.566                | 15.50         | $\pm 0.5$        |

Table 5 – Determined visible spectral lines with corresponding angles from the mercury zinc (Zn)

| Color  | $\lambda$ , nm | $\Delta\lambda$ , nm | Angle, degree | Angle error,min. |
|--------|----------------|----------------------|---------------|------------------|
| red    | 667.8          | 2.229                | 22.42         | $\pm 0.5$        |
| yellow | 587.6          | 2.120                | 21.27         | $\pm 0.5$        |
| yellow | 501.6          | 2.032                | 20.33         | $\pm 0.5$        |
| green  | 492.2          | 1.927                | 19.23         | $\pm 0.5$        |
| green  | 471.3          | 1.778                | 17.68         | $\pm 0.5$        |
| green  | 447.1          | 1.751                | 17.40         | $\pm 0.5$        |
| blue   | 432.5          | 1.699                | 16.87         | $\pm 0.5$        |
| blue   | 428.3          | 1.664                | 16.50         | $\pm 0.5$        |
| blue   | 416.2          | 1.649                | 16.35         | $\pm 0.5$        |
| violet | 411.3          | 1.542                | 15.25         | $\pm 0.5$        |

Intensity maxima occur if the diffraction angle satisfies the following conditions:

$$n\lambda = g\sin\varphi; n = 0, 1, 2\dots \quad (1)$$

Where:  $\lambda$  – wavelength, nm,  $g$  – diffraction grating,  $\varphi$  – the angle of diffraction, deg.

Diffraction grating could be found by rearranging the equation (1) and is calculated using the slope:

$$g = \frac{n\lambda}{\sin\varphi} = \frac{1}{\text{slope}} \quad (2)$$

The diffraction grating constant served as a pivotal parameter for deducing the wavelengths corresponding to the spectral lines of mercury (Hg), cadmium (Cd), and zinc (Zn). Employing Equation (1), with  $n=1$  and  $\varphi$  representing the measured diffraction angles for each spectrum, facilitated the computation of experimental values. Tables 2-5 encompass the resultant experimental data. Specifically, for the determination of experimental mercury (Hg) wavelengths, the diffraction angles were utilized as inputs.

Let's analyze the splitting on the example of the spectral line of the presented lamps, it is possible to note that there is a removal of degeneration of each of the specified levels on quantum number. Thus, the considered spectral line in the presence into three components, which corresponds to the experimental results.

#### 4. Conclusions

The conducted experimental investigation encompassed a meticulous exploration of spectral emissions from various elemental compositions encapsulated within a series of five discrete spectral lamps. This endeavor was facilitated by a comprehensive suite of scientific instrumentation, including an optical spectrometer with converging lenses, a diffraction grating, and ancillary equipment such as a power supply and lamp holder.

Initial calibration of the spectrometer was undertaken utilizing the helium spectral lamp, enabling the determination of diffraction grating parameters. Subsequent spectral analyses involved the measurement of diffraction angles to deduce the wavelengths corresponding to the most intense spectral lines emitted by sodium, mercury, cadmium, and zinc. Notably, the computed diffraction grating constant served as a pivotal parameter in the determination of wavelengths. These experimental findings, compared with theoretical values, facilitated a comprehensive analysis of

observed deviations, which may be attributed to systematic errors introduced during the experiment. Such errors include the influence of extraneous light sources and potential parallax errors in angle measurements. Moreover, examination of spectral line splitting revealed a removal of degeneracy within specified energy levels, resulting in the observation of distinct spectral components. This observation aligns with theoretical expectations and further corroborates the experimental outcomes.

In conclusion, this investigation has provided valuable insights into the spectral characteristics of various elemental compositions, underscoring the importance of meticulous experimental methodologies and the interplay between theory and observation in elucidating fundamental physical phenomena.

## References

1. Empirical Determination of the Bohr-Weisskopf Effect in Cesium and Improved Tests of Precision Atomic Theory in Searches for New Physics / G. Sanamyan, B.M. Roberts, J.S.M. Ginges // *Physical Review Letters*. — 2023. — Vol. 130, No. 5. — P. 053001. <https://doi.org/10.1103/PhysRevLett.130.053001>
2. The theory of the Bohr-Weisskopf effect in the hyperfine structure / F.F. Karpeshin, M.B. Trzhaskovskaya // *Nuclear Physics A*. — 2015. — Vol. 941. — P. 66–77. <https://doi.org/10.1016/j.nuclphysa.2015.06.001>
3. Bohr-Weisskopf effect: Influence of the distributed nuclear magnetization on hfs / H.H. Stroke, H.T. Duong, J. Pinard // *Hyperfine Interactions*. — 2000. — Vol. 129, No. 1–4. — P. 319–335. <https://doi.org/10.1023/A:1012630404421>
4. Atomic beam magnetic resonance apparatus for systematic measurement of hyperfine structure anomalies (Bohr-Weisskopf effect) / H.T. Duong, C. Ekström, M. Gustafsson, T.T. Inamura, P. Juncar, P. Lievens, I. Lindgren, S. Matsuki, T. Murayama, R. Neugart, T. Nilsson, T. Nomura, M. Pellarin, S. Penselin, J. Persson, J. Pinard, I. Ragnarsson, O. Redi, H.H. Stroke, J.L. Vialle // *Nuclear Inst. and Methods in Physics Research, A*. — 1993. — Vol. 325, No. 3. — P. 465–474. [https://doi.org/10.1016/0168-9002\(93\)90392-U](https://doi.org/10.1016/0168-9002(93)90392-U)
5. Bohr-Weisskopf effect: From hydrogenlike-ion experiments to heavy-Atom calculations of the hyperfine structure / B.M. Roberts, P.G. Ranclaud, J.S.M. Ginges // *Physical Review A*. — 2022. — Vol. 105, No. 5. — P. 052802. <https://doi.org/10.1103/PhysRevA.105.052802>
6. Bohr-Weisskopf effect in the potassium isotopes / Y.A. Demidov, M.G. Kozlov, A.E. Barzakh, V.A. Yerokhin // *Physical Review C*. — 2023. — Vol. 107, No. 2. — P. 024307. <https://doi.org/10.1103/PhysRevC.107.024307>
7. Ground-state hyperfine splitting of high-[Formula Presented] hydrogenlike ions / V.M. Shabaev, M. Tomaselli, T. Kühl, A.N. Artemyev, V.A. Yerokhin // *Physical Review A - Atomic, Molecular, and Optical Physics*. — 1997. — Vol. 56, No. 1. — P. 252–255. <https://doi.org/10.1103/PhysRevA.56.252>
8. Thallium hyperfine anomaly | M.G.H. Gustavsson. F. Christian, A.-M. Martensson-Pendrill // *Hyperfine Interactions*. — 2000. — Vol. 127, No. 1–4. — P. 347–352. <https://doi.org/10.1023/A:1012693012231>
9. Calculation of radiative corrections to hyperfine splitting in  $p_{3/2}$  states / J. Sapirstein, K.T. Cheng // *Physical Review A - Atomic, Molecular, and Optical Physics*. — 2008. — Vol. 78, No. 2. — P. 022515. <https://doi.org/10.1103/PhysRevA.78.022515>
10. The Dirac equation in the algebraic approximation: VIII. Comparison of finite basis set and finite element molecular Dirac-Hartree-Fock calculations for the H<sub>2</sub>, LiH, and BH ground states / A.I. Kuleff, Y.I. Delchev, P.Tz. Yotov, Tz. Mineva, J. Maruani // *International Journal of Quantum Chemistry*. — 2002. — Vol. 89, No. 4. — P. 227–236. <https://doi.org/10.1002/qua.10294>

## Information about authors:

*Islam Amangeldinov* – Master Student, Faculty of Engineering and Information Technology, Almaty Technological University, 100 Tole bi st., Almaty, Kazakhstan, [amangeldinovi@list.ru](mailto:amangeldinovi@list.ru)

*Dmitri Korovaev* – MSc, Research Assistant, Institute of Physics, Technical University of Berlin, 17 Straße des, Berlin, Germany, [korovaevdm@gmail.com](mailto:korovaevdm@gmail.com)

## Author Contributions:

*Islam Amangeldinov* – concept, methodology, resources, data collection, testing.

*Dmitri Korovaev* – modeling, analysis, visualization, interpretation, drafting, editing, funding acquisition.

**Conflict of Interest:** The authors declare no conflict of interest.

**Use of Artificial Intelligence (AI):** The authors declare that AI was not used.

*Received: 27.02.2024*

*Revised: 18.04.2024*

*Accepted: 21.04.2024*

*Published: 23.04.2024*



**Copyright:** © 2024 by the authors. Licensee Technobius, LLP, Astana, Republic of Kazakhstan. This article is an open access article distributed under the terms and conditions of the Creative Commons Attribution (CC BY-NC 4.0) license (<https://creativecommons.org/licenses/by-nc/4.0/>).



## Comprehensive analysis of solar cell behavior: effects of light intensity, temperature, and operational modes

 Ersaiyn Bekbolsynov\*

Faculty of Physics and Mathematics, Bukhara State University, 11 Mukhammad Iqbol st., Bukhara, Uzbekistan

\*Correspondence: [ersaiynb@mail.ru](mailto:ersaiynb@mail.ru)

**Abstract.** This study investigates the current-voltage characteristics of a solar cell under varying light intensities, temperatures, and operational conditions to comprehensively assess its performance. The experimental approach involves measuring short-circuit current and open-circuit voltage at different light intensities and constructing current-voltage curves to analyze the solar cell's response to changing illumination levels. The dependence of open-circuit voltage and short-circuit current on temperature is also estimated to understand thermal influences on the solar cell's electrical properties. Additionally, the solar cell's behavior is examined under different operational modes, including cooling with a blower, operation without cooling, and light filtration through a glass plate. The corresponding current-voltage characteristics are plotted to evaluate the impact of thermal management and light modulation on the solar cell's efficiency and stability. Furthermore, the characteristic curve of the solar cell is determined under natural sunlight illumination to simulate real-world conditions. The findings provide valuable insights into optimizing solar cell performance for practical applications and sustainable energy systems. This research contributes to advancing our understanding of solar cell behavior under diverse environmental and operational settings, with implications for enhancing solar energy utilization and promoting renewable energy technologies. Future studies will focus on refining solar cell design and operation based on these insights to maximize efficiency and reliability in solar power generation.

**Keywords:** solar cell, current-voltage characteristics, light intensity, temperature dependence, operational modes, thermal management, renewable energy, sustainability.

### 1. Introduction

Silicon, a fundamental element in the periodic table with the atomic number 14, is widely recognized for its importance in modern technology, particularly in the semiconductor industry. Pure silicon, when isolated and characterized, displays several unique properties essential for its applications in electronics and various scientific endeavors [1]. Pure silicon primarily exists in a crystalline form with a diamond cubic crystal structure. Each silicon atom is covalently bonded to four neighboring silicon atoms, forming a stable and rigid lattice. This crystal structure contributes to silicon's robustness and resilience under varying environmental conditions [2].

One of the most notable properties of silicon is its semiconductor nature [3]. Silicon's electronic properties are influenced by its four valence electrons [4]. At absolute zero temperature, silicon behaves as an insulator due to the completely filled valence band and an empty conduction band. However, at higher temperatures or under specific conditions, silicon can become a semiconductor by promoting electrons from the valence band to the conduction band, thereby facilitating electron mobility crucial for electronic conductivity [5].

To create a  $p$  – or  $n$  – type semiconductor, pure silicon is purposefully "impurified" (doped) with triand pentavalent impurity atoms [6]. The junction formed when  $p$  – and  $n$  – type crystals are combined determines the solar cell's electrical characteristics (Figure 1). When there is no external voltage present and the system is in equilibrium, the Fermi characteristic energy level remains

constant. Electrons diffuse into the  $p$  – region and holes into the  $n$  – region due to the differences in the concentrations of electrons and holes in the two regions. A space charge-limited current area is formed by the immobile impurity atoms, and the diffusion current and the field current balance each other out in an equilibrium [7–9].

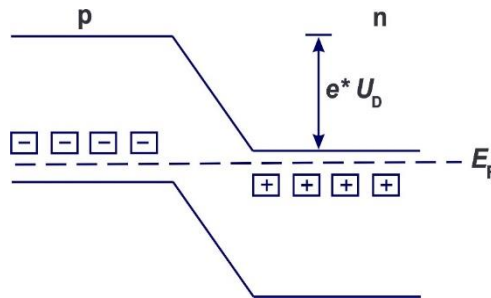


Figure 1 – The energy-band scheme’s + donors and – acceptors are located at the  $pn$  – junction, where  $e$  represents the elemental charge and  $U_D$  is the diffusion potential

The initial disparity in Fermi energy levels between the separate  $p$  – and  $n$  – regions is indicated by the diffusion potential  $U_D$  in the  $pn$  – junction, and this is contingent upon the doping level. In silicon under typical conditions, the gap between the valence and conduction bands is fixed  $E = 1.1 eV$ . The diffusion potential of silicon is between 0.5 and 0.7  $eV$ . The detail construction on Figure 2.

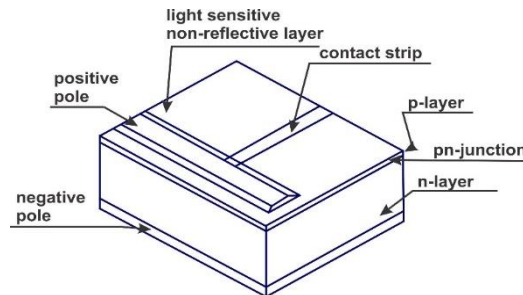


Figure 2 – Putting together a silicon solar cell

Photons from light striking the  $pn$  – junction form electron-hole pairs that are divided by the space charge [10-11]. The  $n$  – region absorbs electrons, while the  $p$  – region absorbs holes. In addition to the  $pn$  – junction, the  $p$  – layer above it also absorbs photons. The generated electrons are minority carriers in those regions because recombination significantly lowers their concentration and, consequently, their efficiency. In order for the electrons of diffusion length  $l_e$  to enter the  $n$  – layer, the  $p$  – layer needs to be thin enough:  $L_E \gg t$ , in a view of the  $t$  is the  $p$  –layer's thickness.

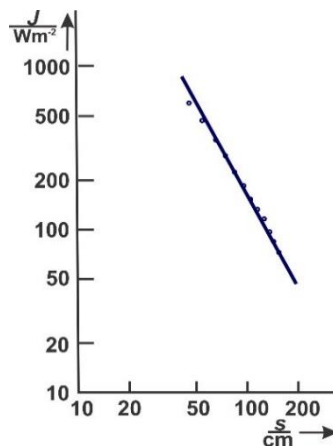


Figure 3 – Intensity of the light at standard distances from the source

When a voltage  $U$  is placed across the  $pn$  – junction and  $g$ , the number of electron-hole pairs generated per unit area, a stream of electrons and holes with a density is formed:

$$i = e * \left( e^{\frac{eU}{kT-1}} \right) * \left( \frac{n_0 D_e t}{L^2 e} + \frac{p_0 D_h}{L_h} \right) - eg \quad (1)$$

When:  $e$  – the elementary charge;  $k$  – Boltzmann's constant;  $T$  – the temperature;  $L$  – the diffusion length of electrons and holes;  $D$  – the diffusion constant for electrons and holes;  $n_0$  and  $p_0$  are equilibrium concentrations of the minority carriers.

At a constant temperature, the short-circuit current density ( $U = 0$ )  $i_s = -e * g$  is proportional to the incident light's intensity. The temperature increases with  $g$  becoming very slightly greater, less than  $10^{-2} \frac{\%}{K}$ . The voltage  $U$  is limited to reaching the same height as the diffusion potential  $U_D$ . The no-load voltage normally drops by  $-2.3 \frac{mV}{K}$  as the temperature rises because the equilibrium concentrations  $n_0$  and  $p_0$  rise with temperature:

$$n_0 \sim e^{-\frac{\Delta E}{2kT}} \quad (2)$$

This research aims to study a solar cell's current-voltage properties at various light intensities. Plot the current-voltage characteristic at various light intensities after measuring the short-circuit current and no-load voltage at various light intensities. Compared to Calculate how temperature affects the short-circuit current and no-load voltage. Additionally, we are interested in experimenting with various modes and plotting the current-voltage characteristic under various operating conditions, such as blower cooling, no cooling, and beaming light through a glass plate. The final step is to identify the characteristic curve under solar illumination.

## 2. Methods

The equipment on which the study was conducted includes a quadruple solar array, in the form of an assembly containing photovoltaic cells for generating electricity from sunlight. A device that converts thermal energy into electrical energy by utilising the Seebeck effect, namely for measuring temperature or generating electricity – a Moll-type thermopile was used as part of all equipment. The solar cell detects stray light from the benchtop reflection in addition to the light from the lamp, which is the only source of light that the thermopile measures. The distance between the light source and the solar cell can be adjusted to change the intensity of the light. Thus, the light intensity was measured using a thermopile and an amplifier at an input voltage of 10 V with equipment at different distances from the light source. To reduce the stray light, a black cloth was placed over the optical bench during the experiment. The change in distance was measured with a 1000 mm metre scale. In this case, the lamp was installed at a distance of 0.5 m from the thermopile due to the fact that the angular aperture of the latter is  $20^\circ$ . The distance between the lamp and the solar panel was more than 0.5 m, as shortening this distance may provoke distortion of the measurement results.

The main characteristics of the solar cell were measured in sunlight; that is, both direct and diffuse light were involved. Thermopile has also been used as a tool to determine the relationship between short-circuit current and light intensity, despite the fact that this equipment is only able to measure direct light due to its small angular aperture. Therefore, for comparative purposes, a black cardboard tube about 20 cm long was fixed in front of the solar cell to shield it from stray light. Thus, the thermopile and solar cell were pointed directly at the sunlight.

An electronic device used to amplify and measure various types of signals, often used in conjunction with sensors or transducers. Also used were 330 Ohm rheostats and a ceramic base designed to accommodate a standard E27 base lamp (e.g. incandescent or LED bulbs) with additional features such as a reflector, switch and protective plug. The source was an incandescent lamp (220 V/120 W) with a reflector. A powerful 1800W blower was used to control the temperature and create hot or cold air. A thermometer with an operating range of  $-10$  to  $+110$  °C was used. It is necessary to blow hot air over the solar cell and record the temperature directly in front of it with a thermometer

to accurately determine the temperature effect. It is important to note that the room temperature of the solar panels and its cells was maintained with a cold air fan. In this case, tactical contact to the cell was excluded, due to the ease of damaging its thin p-layer.

Sturdy bases, tripods, stainless steel support rods of different lengths and flexibility were used to support the entire structure. Different types of clamps were designed to hold rods or other objects at right angles, making complex operations easier. Plate holders have also been used to hold plates securely. In addition, a heavy-duty clamp was used to secure all equipment. Transparent glass panels were selected with a size of 150x100x4 mm. Glass plates were used only to observe the current-voltage relationship under different operating conditions such as fan cooling of the equipment, no cooling, and illumination through the glass plate. An electrical circuit for measuring volt-ampmetered characterisation was assembled as shown in Figure 1. Before experimental procedure the values of the no-load voltage and short-circuit current have been recorded.

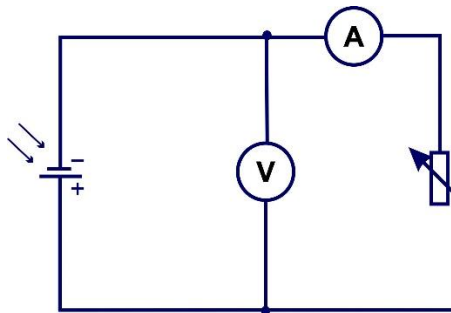


Figure 1 – Electrical circuit for measuring volt-ampmetered characterization

Two digital multimeters were used to measure voltage, current and resistance as well as other electrical parameters such as capacitance, frequency and temperature. Strong electrical cords 500 mm long and 32A amperage connect all parts of the equipment to each other.

### 3. Results and Discussion

For a more accurate and proper experiment, the short-circuit current and no-load voltage at different light intensities were first recorded. Figure 2 shows a plot of current versus voltage at different light intensities. Assume that the measuring surface receives all light that enters the 0.025 m diameter aperture. The graph illustrates a straight line on the graph representing the light intensity  $J$  dependence on distance  $s$ . One can calculate the light intensity at a distance of  $s \leq 0.5$  m by extrapolating the straight line.

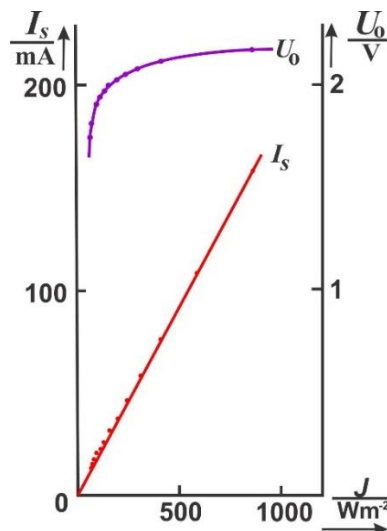


Figure 2 – The relationship between short circuit current and no-load voltage and light intensity



A solar cell with four series-connected cells that have a maximum no-load voltage of 2 V. The sensitivity of the measured equipment reached up to 0.16 mV/mW. Consequently, the intensity of light is described by the following level:

$$I_s = 1.84 * 10^{-4} \frac{A}{Wm^{-2}} * J \quad (3)$$

The values of volt-ampere characteristics were recorded at various light intensities and are displayed in Figure 3. The graph's dotted line connects the turning points of the curves, which represent the places at which the solar cell's internal resistance and the load resistor's values coincide to produce the greatest power production.

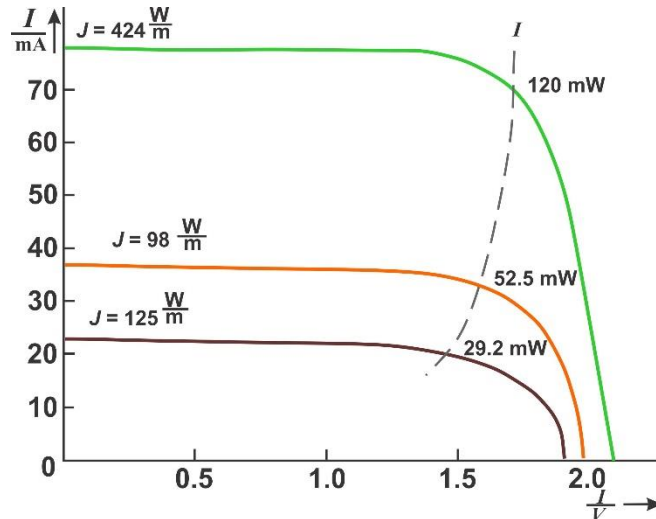


Figure 3 – Characteristics of current and voltage at various light intensities

As a result, as light intensity increases, internal resistance lowers. An efficiency of roughly 6% is obtained when the maximum output power and the incident power are compared, so solar panel area is 0.5 m<sup>2</sup>.

The research has considered the impact of temperature as well as the distribution of temperature over the hot air area. The following equality was obtained by using hot and cold air to measure the no-load voltage:

$$\frac{\Delta U_0}{\Delta T} = -8 \frac{mV}{K} \quad (4)$$

It is important to remember that the measurements can only provide a rough order of magnitude. As a result, we get a value of  $-2 \frac{mV}{K}$  for a single cell. It is impossible to quantify how the short-circuit current changes with temperature.

For completeness of the experimental data, we additionally installed a glass plate, which is able to absorb light in the infrared region and hence used to reduce the temperature rise of the solar cell. Figure 4 is a graph showing the effect of the stack effect work from different ‘modes of operation’. The graph shows three curves: the orange one refers to the fan-cooled mode; the green one indicates the fan-cooled mode; and the blue curve - when shielded with a glass plate. Note that the light intensity in the fan cooling mode is the maximum light intensity.

To identify the difference between different light sources, characteristic curves were recorded when illuminated by sunlight. Figure 5 shows a graph of the dependence of light intensity and wavelength, which shows curves from various sources. The spectral sensitivity of a silicon solar cell and the spectrum of the sun, which has a temperature of around 5800 K, and an incandescent bulb, which has a temperature of about 2000 K. Solar cells produce distinct properties when exposed to sunlight than incandescent lights do:

$$I_s = 3.04 * 10^{-4} \frac{JA}{Wm^{-2}} \quad (5)$$

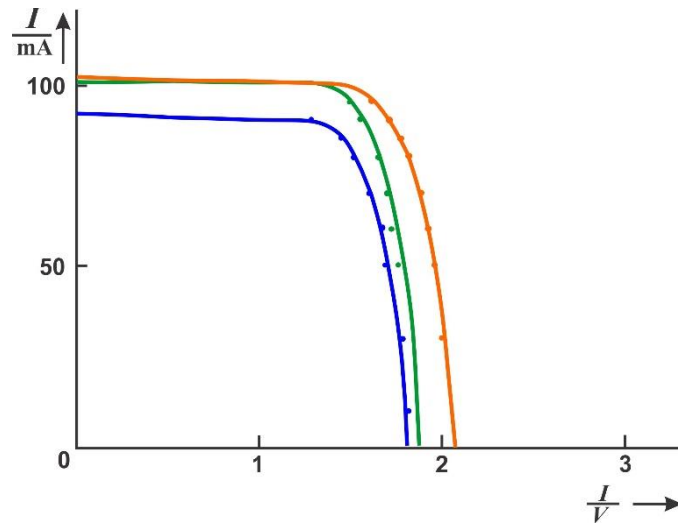


Figure 4 – Characteristics of the solar battery's current and voltage

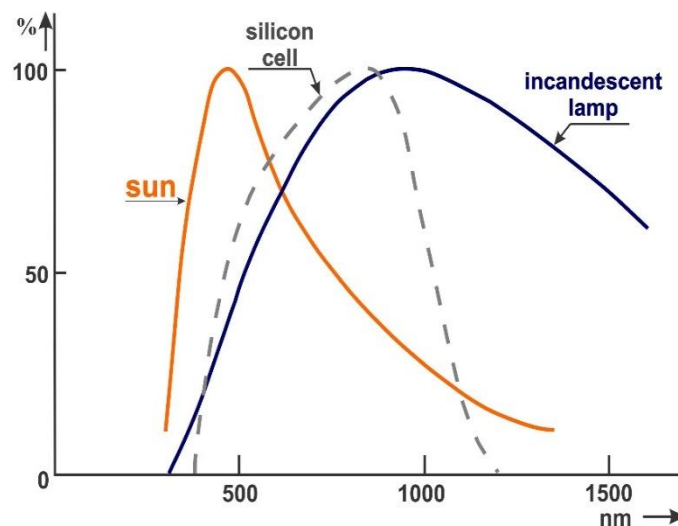


Figure 5 – Spectral characteristics of various sources

The two light sources' different spectra provide the explanation. Light from the sun produces a greater short-circuit current at the same intensity. The solar cell does not heat up as much in the infrared part of the spectrum because of this, and measurements taken with and without cooling provide identical solar properties.

#### 4. Conclusions

This investigation has provided valuable insights into the performance characteristics of a solar cell under varying light intensities, temperatures, and different operational conditions. Initially, the short-circuit current and open-circuit voltage were measured across a range of light intensities, allowing for the construction of current-voltage curves. These curves elucidated the impact of light intensity variations on the electrical output of the solar cell, crucial for understanding its efficiency under changing environmental conditions.

Subsequently, the study estimated the dependence of no-load voltage and short-circuit current on temperature. This analysis highlighted the influence of temperature fluctuations on the solar cell's electrical characteristics, offering insights into its behavior in practical applications.

Furthermore, the investigation evaluated the solar cell's performance under different operating modes, including cooling with a blower, operation without cooling, and light filtration through a glass plate. The corresponding I-V characteristics demonstrated the significance of thermal management and light modulation in optimizing the solar cell's efficiency and stability.

Moreover, the characteristic curve of the solar cell under natural sunlight illumination was determined. This final analysis provided practical data on the solar cell's behavior in real-world conditions, guiding future design and implementation strategies for solar energy systems.

In summary, the findings from this comprehensive study contribute to advancing our understanding of solar cell behavior under diverse environmental and operational settings. This knowledge is instrumental in improving the efficiency, reliability, and practicality of solar energy technologies, paving the way for sustainable and effective solar power generation systems. Continued research in this field will further refine our ability to harness solar energy for a cleaner and more sustainable future.

### References

1. Note on the properties of silicon / R. Hare // Journal of the Franklin Institute. — 1833. — Vol. 15, No. 6. — P. 362–363. [https://doi.org/10.1016/s0016-0032\(33\)90307-5](https://doi.org/10.1016/s0016-0032(33)90307-5)
2. Space radiation applicability of pure silicon-core optical fibers / J. Xiao, Z. Hengjing, Zh. Hongqi, M. Xiping, J. Qiuyang // Infrared and Laser Engineering. — 2017. — Vol. 46, No. 8. — P. 822002. <https://doi.org/10.3788/irla201746.0822002>
3. The semiconductor silicon industry roadmap: Epochs driven by the dynamics between disruptive technologies and core competencies / S.T. Walsh, R.L. Boylan, C. McDermott, A. Paulson // Technological Forecasting and Social Change. — 2005. — Vol. 72, No. 2. — P. 213–236. [https://doi.org/10.1016/S0040-1625\(03\)00066-0](https://doi.org/10.1016/S0040-1625(03)00066-0)
4. Amorphous silicon enhanced metal-insulator-semiconductor contacts for silicon solar cells / S.L. Zhang, J. Shao, L.S. Hoi, S.N. Wu, B.F. Zhu, F. Shou-Shan, H.D. Li, D.P. Yu // Physica Status Solidi C: Conferences. — 2005. — Vol. 2., No. 8. — P. 3090–3095. <https://doi.org/10.1002/pssc.200460765>
5. Silicon-doped carbon semiconductor from rice husk char / S. Maiti, P. Banerjee, S. Purakayastha, B. Ghosh // Materials Chemistry and Physics. — 2008. — Vol. 109, No. 1. — P. 169–173. <https://doi.org/10.1016/j.matchemphys.2007.11.011>
6. Solid-state physics: Super silicon / R.J. Cava // Nature. — 2006. — Vol. 444, No. 7118. — P. 427–428. <https://doi.org/10.1038/444427a>
7. Carrier heating and its effects on the current-voltage relations of conventional and hot-carrier solar cells: A physical model incorporating energy transfer between carriers, photons, and phonons / C.-Y. Tsai // Solar Energy. — 2019. — Vol. 188. — P. 450–463. <https://doi.org/10.1016/j.solener.2019.06.024>
8. Electrical characteristics and hot carrier effects in quantum well solar cells / D.-T. Nguyen, L. Lombez, F. Gibelli, M. Paire, S. Boyer-Richard, O. Durand, J.-F. Guillemoles // Proceedings of SPIE - The International Society for Optical Engineering. — 2017. — Vol. 10099. — P. 127693. <https://doi.org/10.1117/12.2251331>
9. Direct measurement of the internal electron quasi-fermi level in dye sensitized solar cells using a titanium secondary electrode / K. Lobato, L.M. Peter, U. Würfel // Journal of Physical Chemistry B. — 2006. — Vol. 110, No. 33. — P. 16201–16204. <https://doi.org/10.1021/jp063919z>
10. The open-circuit voltage in microcrystalline silicon solar cells of different degrees of crystallinity / M. Nath, P. Roca i Cabarrocas, E.V. Johnson, A. Abramov, P. Chatterjee // Thin Solid Films. — 2008. — Vol. 516, No. 20. — P. 6974–6978. <https://doi.org/10.1016/j.tsf.2007.12.052>
11. Solar energy conversion with hot electrons from impact ionisation / P. Würfel // Solar Energy Materials and Solar Cells. — 1997. — Vol. 46, No. 1. — P. 43–52. [https://doi.org/10.1016/S0927-0248\(96\)00092-X](https://doi.org/10.1016/S0927-0248(96)00092-X)

### Information about author:

*Ersaiyn Bekbolsynov* – Master Student, Faculty of Physics and Mathematics, Bukhara State University, 11 Mukhammad Iqbol st., Bukhara, Uzbekistan, [ersaiynb@mail.ru](mailto:ersaiynb@mail.ru)

### Author Contribution:

*Ersaiyn Bekbolsynov* – concept, methodology, resources, data collection, testing, modeling, analysis, visualization, interpretation, drafting, editing, funding acquisition.

**Conflict of Interest:** The authors declare no conflict of interest.

**Use of Artificial Intelligence (AI):** The authors declare that AI was not used.

*Received: 09.03.2024*

*Revised: 25.04.2024*

*Accepted: 01.05.2024*

*Published: 03.05.2024*



**Copyright:** © 2024 by the authors. Licensee Technobius, LLP, Astana, Republic of Kazakhstan. This article is an open access article distributed under the terms and conditions of the Creative Commons Attribution (CC BY-NC 4.0) license (<https://creativecommons.org/licenses/by-nc/4.0/>).



Article

## Cooling and heating innovations: exploring the diverse applications of heat pumps

 Aliya Nurbayeva,  Karina Mussabekova\*

Faculty of Mechanical Engineering, Energy and Information Technologies, Akhmet Baitursynuly Kostanay Regional University, 47 Baytursynov st., Kostanay, Kazakhstan

\*Correspondence: [karina.mussabekova@mail.ru](mailto:karina.mussabekova@mail.ru)

**Abstract.** Heat pumps are versatile and energy-efficient devices that play a crucial role in modern heating, cooling, and refrigeration applications. This work provides a concise overview of the diverse applications and benefits of heat pumps across residential, commercial, industrial, and transportation sectors. The paper discusses the principles of heat pump operation, emphasizing their capability to transfer heat from one location to another using thermodynamic processes. This work highlights key applications such as residential heating, ventilation, and air conditioning systems, commercial refrigeration, hot water heating, process cooling, and renewable energy integration. The energy efficiency and environmental benefits of heat pumps are also emphasized, showcasing their potential to reduce carbon emissions and contribute to sustainable energy practices. By understanding the broad scope of heat pump applications outlined in this paper, researchers, engineers, policymakers, and industry stakeholders can gain insights into the significance of heat pump technology in advancing energy efficiency and addressing climate change challenges.

**Keywords:** heating, ventilation, air conditioning, temperature control, humidity regulation, energy efficiency.

### 1. Introduction

Heat pumps have emerged as essential and versatile technologies in modern heating, cooling, and refrigeration applications across residential, commercial, industrial, and transportation sectors [1]. These devices utilize thermodynamic principles to transfer heat from one location to another, providing efficient and environmentally friendly solutions for space conditioning and temperature control [2].

In recent years, the adoption of heat pumps has increased significantly due to their energy efficiency, reduced environmental impact, and versatility in diverse applications [3–6]. This article explores the wide-ranging applications of heat pumps, highlighting their role in residential heating and cooling, commercial HVAC systems, refrigeration, hot water heating, process cooling, and renewable energy integration.

The Peltier effect is based on the principles of thermoelectricity, which involves the conversion of temperature differences into electric voltage (Seebeck effect) and vice versa (Peltier effect) [7–9]. This effect has practical applications in thermoelectric cooling devices, such as portable refrigerators, where it is used for efficient heat pumping without the need for moving parts like compressors, making it a key technology in various industries ranging from consumer electronics to scientific instrumentation (Figure 1).

This effect describes the heating or cooling of a junction of two dissimilar conductors or semiconductors when an electric current is passed through them. When current flows through the junction, heat is either absorbed or released, depending on the direction of the current:

$$\frac{Q}{t} = P_p = \pi * I = \alpha * T * I \quad (1)$$

Where  $\pi$  is the Peltier coefficient, the  $\alpha$  is the Seebeck coefficient [10] and  $T$  is the absolute temperature. Heat will either be absorbed or released in a homogeneous conductor when an electric current  $T$  runs in the direction of a temperature gradient  $\frac{dT}{dx}$ , depending on the material (Thomson effect):

$$P_T = \tau * I * \frac{dT}{dx} \tag{2}$$

Where  $\tau$  is the Thomson coefficient. Figure 2 demonstrate a Peltier element is typically made from two different types of semiconductor materials, often bismuth telluride  $Bi_2Te_3$  or other similar materials with high thermoelectric efficiency [11-12]. The semiconductor material is doped to create two types of regions: N-type (electron-rich) and P-type (hole-rich). These regions are arranged to create multiple P-N junctions, which are crucial for the Peltier effect.

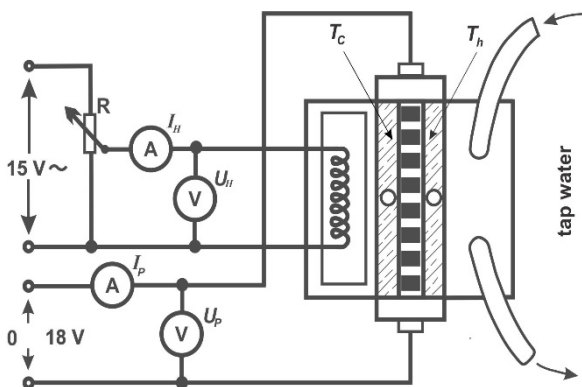


Figure 1 – Configuration to ascertain cooling capability

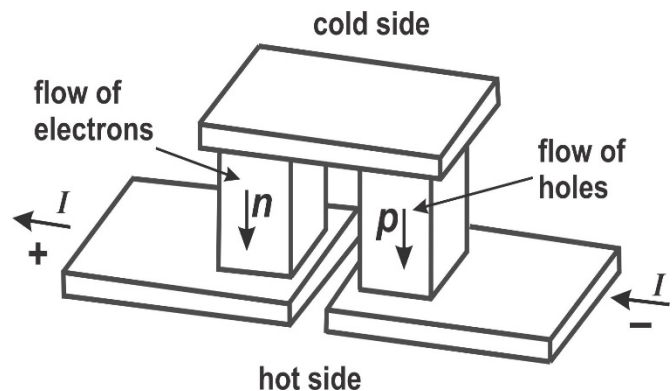


Figure 2 – Building a semi-conductor Peltier element: in actuality, a number of parts are typically connected both thermally and electrically in parallel

Figure 3 is a power balance block diagram for a Peltier component including an illustration of how electrical energy is converted into thermal energy and the cooling effect within the device [13-14].

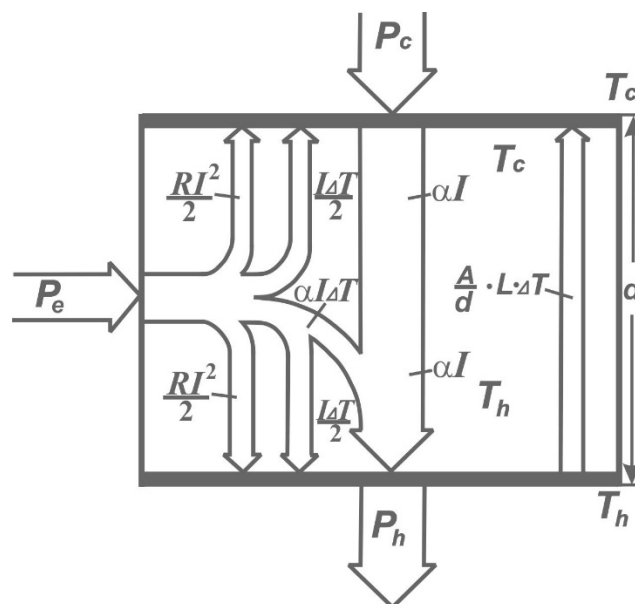


Figure 3 – A Peltier component's power balance flow diagram, that provided relates to the scenario in which  $PT > 0$

The Peltier component is powered by an electrical input, typically from a DC power source. The input electrical power is the energy provided to the Peltier device. The Peltier effect occurs at the

junctions of the Peltier device, where heat is either absorbed or released depending on the direction of the electric current. One side of the Peltier device absorbs heat from the surroundings. This side becomes cooler. The other side of the Peltier device rejects heat into the surroundings. This side becomes warmer. The absorbed heat results in cooling of one side of the Peltier device, achieving the desired cooling effect. The rejected heat increases the temperature of the opposite side of the Peltier device. The Peltier device facilitates the transfer of heat from one side to the other, depending on the direction of the electric current. The net effect is the generation of cooling on one side and heating on the other side of the Peltier device, allowing for precise temperature control and thermal management [15-16].

The sign of the Thomson coefficient, the direction of the temperature gradient, and the direction of the current all influence which way heat moves. The Joule effect occurs when an electric current  $I$  runs through an isothermal conductor with resistance  $R$ :

$$P_j = R * I^2 \quad (3)$$

Heat also transfers from the hot side  $T_h$  to the cold side  $T_c$  due to heat conduction:

$$P_L = L \frac{A}{d} (T_h - T_c) \quad (4)$$

Where  $A$  is the cross-sectional area,  $d$  is the thickness of the Peltier component, and  $L$  is the conductivity.

By  $\Delta T = T_h - T_c$ , it can be derived the following for the pump's cold-side heat capacity (also known as its cooling capacity):

$$-P_c = \alpha T_c I \pm \frac{\tau I \Delta T}{2d} - \frac{1}{2} I^2 R - \frac{L A \Delta T}{d} \quad (5)$$

Additionally, regarding the hot side pump's heat capacity:

$$+P_h = \alpha T_h I \pm \frac{\tau I \Delta T}{2d} - \frac{1}{2} I^2 R - \frac{L A \Delta T}{d} \quad (6)$$

The electricity that is provided is:

$$+P_{el} = \alpha \Delta T I \pm \frac{\tau I \Delta T}{2d} - I^2 R = U_p * I_p \quad (7)$$

The objective of this experimental investigation is to explore the operational characteristics of a Peltier heat pump. The study aims to accomplish several specific goals: firstly, to ascertain the cooling capacity of the pump as a variable function of applied current; secondly, to compute the efficiency rating of the heat pump under conditions of maximum cooling output. Additionally, the investigation seeks to determine the heating capacity of the pump and its corresponding efficiency rating under conditions of sustained current and a consistent temperature on the cold side.

Moreover, the study endeavors to establish the time-dependent behaviors of temperature across the hot and cold sides of the heat pump, discerning pertinent relationships between these variables. Specifically, the experiment aims to characterize the temporal evolution of temperature on both sides during operational phases.

Furthermore, an examination of the temperature dynamics during cooling operations is intended, particularly focusing on the air-cooled condition of the hot side of the heat pump. This investigation will provide insights into the thermal behaviors and operational constraints of the Peltier heat pump system in the context of cooling applications.

By understanding the varied applications and benefits of heat pumps, stakeholders in the energy and HVAC industries can make informed decisions about deploying these technologies to achieve energy savings, improve thermal comfort, and contribute to sustainable practices. This article aims to provide a comprehensive overview of heat pump applications, emphasizing their importance in advancing energy-efficient solutions and mitigating climate change challenges.

## 2. Methods

We have assembled an improved experimental setup for accurate thermal experiments and measurements, which includes: thermogenerator with 2 water baths; flow-through heat exchanger,

which allows for controlled heat exchange processes, crucial for studying fluid dynamics and thermodynamics; an apparatus designed to rapidly cool gases or liquids, providing a means to investigate cooling processes and heat dissipation; heating coil with sockets, that utilized for generating and controlling heat through electrical resistance, enabling varied heat settings for experimental setups.

The installation also included distributor, which used to evenly distribute fluids or gases, ensuring uniformity in experimental conditions; a precision variable resistor (33 Ohm, 3.1A) employed for adjusting current flow in electrical circuits, essential for fine-tuning heating elements; capable of delivering both DC (0-18 V, 0-5 A) and AC (2/4/6/8/10/12/15 V, 5 A) currents, facilitating a wide range of electrical experiments; Power supply, universal DC: 0...18 V, 0...5 A / AC: 2/4/6/8/10/12/15 V, 5 A, four high-precision instruments for measuring voltage (up to 600V AC/DC), current (up to 10A AC/DC), resistance (up to 20 MΩ), capacitance (up to 200 μF), frequency (up to 20 kHz), and temperature (from -20°C to 760°C); A multifunctional timer with precision down to 1/100 second, essential for timing experiments accurately; A powerful device (1800 W) capable of generating controlled streams of hot or cold air for thermal studies; several thermometers calibrated for different temperature ranges (-10°C to +110°C and -10°C to +50°C), crucial for monitoring and recording experimental temperatures; with an internal diameter of 6 mm, used for connecting different components in fluid systems.

All equipment was held by essential's powerful apparatus to fix and stabilise the experimental setups like universal clamp, tripod base, support rod, stainless steel,  $l = 250$  mm,  $d = 10$  mm.; a specialized clamp for securely holding equipment at right angles, ensuring stability during experiments. A variety of heavy-duty connection cords (32 A) in different lengths and colours (red and blue), ensured safe and efficient electrical connections. During the experiment, we used heat conductive paste to increase the thermal conductivity between the surfaces, ensuring efficient heat transfer in the units.

On the cold side, a water bath was erected, and on the hot side, a heat exchanger that allows tap water to flow through was installed. An alternating current heating coil with a resistance of roughly 3 Ohm was submerged in a water-filled bath. Using a rheostat  $R$ , the heating power  $P_H = U_H * I_H$  was adjusted for each value of current  $I_p$  to ensure that there was little to no temperature differential between the hot and cold sides. in which instance the power supplied and the cooling power are exactly identical. The temperatures of the hot side  $T_h$  and the cold side  $T_c$  were recorded, together with the values of the heater current  $I_h$ , voltage  $U_h$ , operational current  $I_p$ , and voltage  $U_p$ .

Then, the heating coil was removed. Now that the operational current was flowing in the opposite direction, the bath water was heated. At constant current  $I_p$ , the values of the water's temperature rise ( $T_W$ ) were noted. Additionally, the temperature rise  $T_C$  was measured. Determine the heat capacities of the brass bath  $C_{BR}$ , the water  $C_W$ , and the copper block  $C_{CU}$  using their respective weights or dimensions.

Subsequently, water baths were erected on either side of the heat pump and loaded with uniformly heated water. At a constant current  $I_P$ , the temperature variations of the two water baths were recorded:

$$T_h = f(t), T_c = f(t), I_p, U_p \quad (8)$$

The air cooler is on the hot side and the water bath is on the cold side in the fourth experiment. In two different regimes—when the cooler is in static atmospheric air and when it is forcefully cooled by a blower—the temperature of the cold side was measured as a function of time.

### 3. Results and Discussion

By determining the cooling capacity  $P_C$  of the pump as a function of the current, it can be assessed how effectively  $\eta_C$  the pump transfers heat from the system it is cooling. The cooling capacity (in watts) provides a quantitative measure of the pump's ability to remove heat, which is



crucial for applications where temperature control is essential (e.g., in HVAC systems, refrigeration, or thermal management of electronic devices).

In the experimental investigation, the cooling capacity  $P_C$  of the pump was determined to be 49 W under the condition where the pump current  $I_P$  was set at 5 A and the input power  $P_h$  equaled the cooling power  $P_C$ . This finding represents a quantitative measure of the pump's ability to remove heat from the system at the specified operating parameters. This dependence is presented visually in Figure 4.

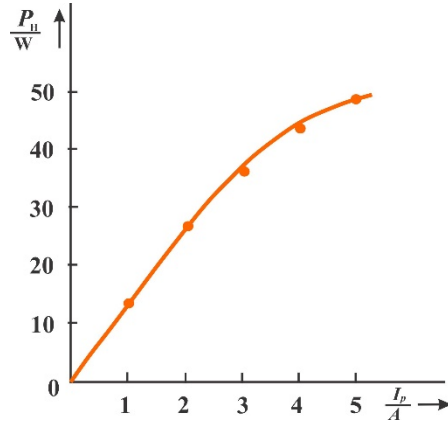


Figure 4 – The relationship between the operating current and pump cooling capacity

Calculated efficiency factor supplied by formula:

$$\eta_C = \frac{P_C}{P_{el}} \quad (9)$$

Using the measured values  $I_P = 5$  A,  $U_P = 14.2$  V and  $\eta_C = 0.69$  (with  $v_h = v_c = 20^\circ\text{C}$ ).

Understanding the heating capacity helps evaluate how much heat the pump can generate under specific operating conditions. This information is crucial for assessing the pump's performance in heating applications, such as in thermal management systems or heating devices. A plot of the hot side temperature versus time is shown in Figure 5.

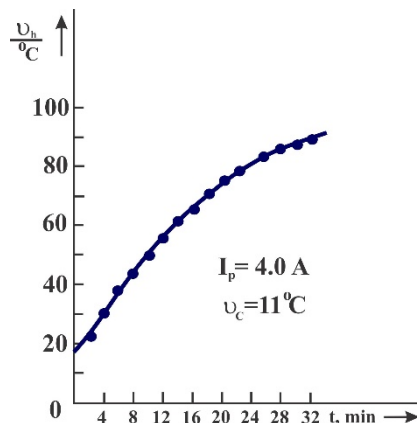


Figure 5 – The relationship of hot side temperature and time

Pump heating capacity can be computed from the slope of the curve in Figure 5, where the curve begins as a straight line or by the formula. To calculate the heating capacity and efficiency at constant current  $I_C$  and constant temperature on the cold side  $T_C$ , we need to consider the heat transfer processes involved in the pump's operation. The heating capacity can be determined by the electrical power input  $P_{el}$ , and the efficiency can be calculated using the output heating power  $Q$  and the electrical input power:

$$P_h = \frac{c_{tot}\Delta T_h}{\Delta T} \quad (10)$$

The corresponding efficiency score was calculated using formula 9, with  $P_{el} = I_p * U_p$ , corresponding results in Table 1.

Table 1 – Calculated results for pump heating

| Type         | m, kg  | $C, \frac{J}{kg \cdot K}$ |
|--------------|--------|---------------------------|
| Water        | 0.194  | 4182                      |
| Brass        | 0.0983 | 381                       |
| Copper block | 0.712  | 383                       |

$$C_{tot} = m_W * C_W + m_{Br} * C_W + m_{CU} * C_{CU} = 1121 \frac{J}{kg \cdot K} \quad (11)$$

Through the slope on the graph of Figure 2 we also obtained  $\frac{\Delta T_h}{\Delta T} = 6.7 * 10^{-2}$  and  $P_h = 75 W$ . The efficiency at average values  $I_p$  of 4.0 A and  $U_p$  of 12.5 V was  $\eta_C = 1.5$ .

We also investigated the water temperature as a function of time, a graph of which can be seen in Figure 6. Measurements were taken for 24 seconds. The influence of the cooling mode on the result has led us to study this aspect. Figure 7 shows two curves relating the temperature of water that was subjected to hot-side cooling with an air cooler an air cooler (curve a) and cooled by convection (curve b), i.e. forced cooling.

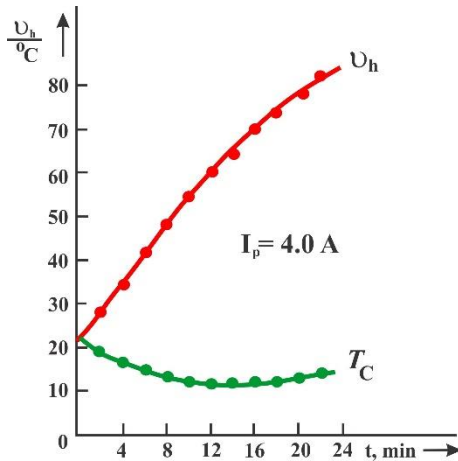


Figure 6 –  $T_w$  as a function of time

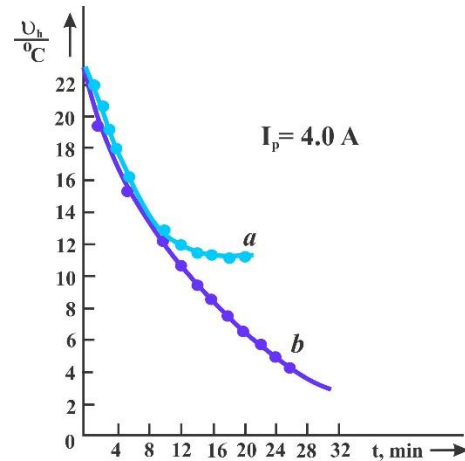


Figure 7 –  $T_w$  after using an air cooler to cool the hot side: a) convection cooling; b) forced cooling

$P_h$  and  $P_c$  and  $\eta_h$  and  $\eta_c$  can be calculated from the slopes of the curves  $v_h = f(t)$  and  $v_c = f(t)$  the relevant heat capacities.

With  $\frac{\Delta v_h}{\Delta t} = 0.056 \frac{K}{s}$  (start of curve) and  $\frac{c \Delta v_c}{\Delta t} = -0.023 \frac{K}{s}$  and  $C_{tot} = 1121 \frac{J}{K}$ , we obtain:  $P_h = 63 W$  and  $P_c = 26 W$ . In the range considered  $U_p$ , the voltage was 12.4 V, so that we obtain the efficiency ratings  $\eta_h = 1.3$  and  $\eta_c = 0.52$  ( $I = 4 A$ ,  $T = 22 \text{ }^\circ\text{C}$ ).

The temperature changes that were seen in the cold side of the water bath when the hot side was cooled with an air cooler are depicted in Figure 7. After 20 minutes, the hot side temperature first dropped to about  $72^\circ\text{C}$  without the fan. When the maximum temperature differential was reached as a result of this decrease, the Peltier pump's power output decreased to zero. On the other hand, the hot side's temperature steadied after the fan was turned on, and after 20 minutes, it remained at about  $45^\circ\text{C}$ .

#### 4. Conclusions

In conclusion, the experimental investigation of the Peltier heat pump has provided valuable insights into its cooling and heating capacities under specific operating conditions. By determining

the cooling capacity as a function of the current, the efficiency of the pump in transferring heat from the cooled system can be evaluated. The cooling capacity serves as a quantitative measure of the pump's ability to remove heat, which is essential for applications requiring precise temperature control, such as HVAC systems, refrigeration, or electronic device cooling.

In this study, the cooling capacity of the pump was determined to be 49 watts at a pump current of 5 amperes, where the input equaled the cooling power. This finding represents a significant parameter in assessing the effectiveness of the pump under specified operational parameters.

Furthermore, understanding the heating capacity of the pump is crucial for evaluating its performance in heating applications. The heating capacity quantifies the amount of heat the pump can generate under specific conditions. The plot of hot side temperature versus time allows for the computation of heating capacity from the slope of the curve. This information is vital for optimizing thermal management systems and heating devices utilizing Peltier heat pump technology.

To further analyze the heating capacity and efficiency at constant current and constant temperature on the cold side, the heat transfer processes involved in the pump's operation must be considered. Table 1 presents calculated results for pump heating, including specific heat capacities for different materials used in the experimental setup (water, brass, and copper block). These values facilitate the evaluation of heat transfer characteristics and efficiency within the Peltier heat pump system.

In summary, the experimental investigation outlined in this study contributes valuable data and insights into the operational capabilities and performance metrics of Peltier heat pumps, which are instrumental in advancing thermal management technologies for various industrial and consumer applications.

## References

1. Experimental investigation of a novel thermal energy storage unit in the heat pump system / M. Koşan, M. Aktaş // Journal of Cleaner Production. — 2021. — Vol. 311. — P.127607. <https://doi.org/10.1016/j.jclepro.2021.127607>
2. Thermal performance evaluation of multi-tube cylindrical LHS system / B.G. Abreha, P. Mahanta, G. Trivedi // Applied Thermal Engineering. — 2020. — Vol. 179. — P. 115743 <https://doi.org/10.1016/j.applthermaleng.2020.115743>
3. Phase change storage solar heat pump hydronics based on cloud computing / W. WU // Thermal Science. — 2024. — Vol. 28, No. 2B. — P. 1423–1429. <https://doi.org/10.2298/TSCI2402423W>
4. Total energy heat pump / Y.H.V. Lun, S.L.D. Tung // Green Energy and Technology. — 2020. — P. 65–79. [https://doi.org/10.1007/978-3-030-31387-6\\_5](https://doi.org/10.1007/978-3-030-31387-6_5)
5. Performance comparison of single-stage/cascade heat pump for waste heat recovery of printing-dyeing industry / D. Gu, Y. Yang, Y. Wu, W. Yan, B. Hu, L. Shi, C. Shen, M. Chen, C. Zheng, Y. Cai, W. Li // Second International Conference on Energy, Power, and Electrical Technology (ICEPET 2023). — 2023. — Vol. 12788. — P. 3004469. <https://doi.org/10.1117/12.3004469>
6. Analysis of a solar-assisted heat pump system with hybrid energy storage for space heating / S. Zhang, S. Liu, J. Wang, Y. Li, Z. Yu // Applied Thermal Engineering. — 2023. — Vol. 231. — P. 120884. <https://doi.org/10.1016/j.applthermaleng.2023.120884>
7. Peltier effect: From linear to nonlinear / Z. Yang, C. Zhu, Y.-J. Ke, X. He, F. Luo, J. Wang, J.-F. Wang, Z.-G. Sun // Wuli Xuebao/Acta Physica Sinica. — 2021. — Vol. 70, No. 10. — P. 1826. <https://doi.org/10.7498/aps.70.20201826>
8. Theoretical and Experimental Investigation about the Influence of Peltier Effect on the Temperature Loss and Performance Loss of Thermoelectric Generator / X. Li, J. Wang, Q. Meng, D. Yu // Energy Technology. — 2022. — Vol. 10, No. 4. — P. 895. <https://doi.org/10.1002/ente.202100895>
9. Improvement of the Self-Heating Performance of an Advanced SiGe HBT Transistor through the Peltier Effect / A. Boulgheb, M. Lakhdara, S. Latreche // IEEE Transactions on Electron Devices. — 2021. — Vol. 68, No. 2. — P. 479–484. <https://doi.org/10.1109/TED.2020.3044869>
10. Portable Thermal Electricity Generator Using the Seebeck Effect of Peltier as an Alternative Energy / Habibullah, Hastuti, T. Muhammad, D.S. Putra, J. Sardi // 2023 International Conference on Advanced Mechatronics, Intelligent Manufacture and Industrial Automation, ICAMIMIA 2023 – Proceedings. — 2023. — Vol. 1. — P. 564–568. <https://doi.org/10.1109/ICAMIMIA60881.2023.10427831>
11. Thermoregulation of Smart Clothing based on Peltier Elements / M.F. Mitsik, M.V. Byrdina // 2020 IEEE East-West Design and Test Symposium, EWDTs 2020 - Proceedings. — 2020. — Vol. 4. — P. 164143. <https://doi.org/10.1109/EWDTs50664.2020.9224805>

12. Peltier elements vs. heat sink in cooling of high power LEDs / N. Bădălan, P. Svasta // Proceedings of the International Spring Seminar on Electronics Technology. — 2015. — Vol. 2015 – September. — P. 124–128. <https://doi.org/10.1109/ISSE.2015.7247975>
12. Peltier elements vs. heat sink in cooling of high power LEDs / N. Bădălan, P. Svasta // Proceedings of the International Spring Seminar on Electronics Technology. — 2015. — Vol. 2015 – September. — P. 124–128. <https://doi.org/10.1109/ISSE.2015.7247975>
13. The central role of the Peltier coefficient in thermoelectric cooling / J. Garrido, A. Casanovas // Journal of Applied Physics. — 2014. — Vol. 115, No. 12. — P. 123517. <https://doi.org/10.1063/1.4869776>
14. Peltier modules in cooling systems for electronic components / K. Domke, P. Skrzypczak // Advanced Computational Methods and Experiments in Heat Transfer XI. — 2010. — Vol. 68. — P. 3–12. <https://doi.org/10.2495/HT100011>
15. Dismantling and chemical characterization of spent Peltier thermoelectric devices for antimony, bismuth and tellurium recovery / M. Balva, S. Legeai, L. Garoux, N. Leclerc, E. Meux // Environmental Technology (United Kingdom). — 2017. — Vol. 38, No. 7. — P. 791–797. <https://doi.org/10.1080/09593330.2016.1211748>
16. Direct observation of the spin-dependent Peltier effect / J. Flipse, F.L. Bakker, A. Slachter, F.K. Dejene, B.J. Van Wees // Nature Nanotechnology. — 2012. — Vol. 7, No. 3. — P. 166–168. <https://doi.org/10.1038/nnano.2012.2>

### Information about authors:

*Aliya Nurbayeva* – Master Student, Faculty of Mechanical Engineering, Energy and Information Technologies, Akhmet Baitursynuly Kostanay Regional University, 47 Baytursynov st., Kostanay, Kazakhstan, [alya.nurbayeva@mail.ru](mailto:alya.nurbayeva@mail.ru)

*Karina Mussabekova* – Master Student, Faculty of Mechanical Engineering, Energy and Information Technologies, Akhmet Baitursynuly Kostanay Regional University, 47 Baytursynov st., Kostanay, Kazakhstan, [karina.mussabekova@mail.ru](mailto:karina.mussabekova@mail.ru)

### Authors Contribution:

*Aliya Nurbayeva* – concept, methodology, resources, data collection, testing, modeling.

*Karina Mussabekova* – analysis, visualization, interpretation, drafting, editing, funding acquisition.

**Conflict of Interest:** The authors declare no conflict of interest.

**Use of Artificial Intelligence (AI):** The authors declare that AI was not used.

*Received:* 01.03.2024

*Revised:* 27.04.2024

*Accepted:* 01.05.2024

*Published:* 03.05.2024



**Copyright:** © 2024 by the authors. Licensee Technobius, LLP, Astana, Republic of Kazakhstan. This article is an open access article distributed under the terms and conditions of the Creative Commons Attribution (CC BY-NC 4.0) license (<https://creativecommons.org/licenses/by-nc/4.0/>).